Title
Towards Closed-Loop Neuromodulation with Wireless Biomimetic Circuits and Systems

Author
Wang, Po-Min

Publication Date
2019

Peer reviewed|Thesis/dissertation

UNIVERSITY OF CALIFORNIA

Los Angeles

Towards Closed-Loop Neuromodulation with Wireless Biomimetic Circuits and Systems

A dissertation submitted in partial satisfaction of the

requirements for the degree Doctor of Philosophy

in Bioengineering

by

Po-Min Wang

2019

ABSTRACT OF THE DISSERTATION

Towards Closed-Loop Neuromodulation with Wireless Biomimetic Circuits and Systems

by

Po-Min Wang

Doctor of Philosophy in Bioengineering

University of California, Los Angeles, 2019

Professor Wentai Liu, Chair

Conventional functional electrical stimulation for neuromodulation delivers regular and periodic electrical pulses in an open-loop fashion. However, with advances in neuroscience, emerging applications require an electrical stimulation delivered in a non-conventional form. For example, electroceuticals and brain-machine interface (BMI) need a closed-loop modulation scheme such that the stimulation protocol can be dynamically adjusted in response to the subject's physiological state. Furthermore, it has been recently shown that a stimulation pattern that mimics the biological signal (i.e. biomimetic stimulation) outperforms periodic pulses in some applications including retina stimulation to regain eyesight and spinal cord stimulation to restore motor function. Despite increasing interests in closed-loop neuromodulation and biomimetic stimulation,

existing implantable neuromodulation devices have limited capability in supporting those sophisticated stimulation schemes.

We have developed two wireless biomimetic systems—an implantable stimulation and recording system and a biomimetic stimulation system, aiming to support closed-loop neuromodulation and biomimetic stimulation. In this dissertation, system design and circuit implementation of both systems are presented. Both systems were validated in bench-top tests and *in-vivo* experiments. The implantable system was used to conduct intestinal stimulation that facilitated the intestinal transit in chronic porcine experiments. The implant is an order lighter and 7.7 times smaller than commercialized GI stimulators, and the delivered electrical charge is smaller than most existing protocols, thus safer and more energy-efficient. The system was also used to conduct acute epidural stimulation in rat models and selectively activate desired muscles through targeting different motor neurons, laying the foundation for the future development of the control algorithms for closed-loop epidural stimulation. On the other hand, the biomimetic stimulation system was also validated in acute experiments using spinally transected rats. The system that delivered a protocol mimicking electromyography (EMG) signal lowered the excitation threshold of the spinal network, showing its potential of accelerating the rate of functional recovery after spinal cord injury. The development of these two biomimetic systems along with the future implementation of the closed-loop control algorithm using the *in-vivo* data acquired by both systems will make an implantable device that supports closed-loop biomimetic stimulation a reality.

The dissertation of Po-Min Wang is approved.

Daniel T. Kamei

Pei-Yu Chiou

Hsian-Rong Tseng

Wentai Liu, Committee Chair

University of California, Los Angeles

2019

Table of Contents

Abstract……..……..…….ii

Table of Contents v

List of Figures vii

List of Tables xiii

Acknowledgment xiv

Biographical Sketch xvi

Chapter 1 Introduction 1

Chapter 2 Design of Wireless Biomimetic Circuits and Systems 4

2.1 Implantable Stimulation and Recording System 4

2.1.1 System Overview 4

2.1.2 Miniaturized Bioelectronic Implant 6

2.1.2.1 System on a Chip (SoC) 6

2.1.2.2 Thin-Film Electrode Array and Heterogeneous Packaging 10

2.1.3 Rendezvous Device 12

2.2 Biomimetic Stimulation System 19

2.2.1 Background 19

2.2.2 System Overview 22

2.2.3 Design and Implementation 23

Chapter 3 Bench-top Test Results 27

3.1 Bench-Top Test of the Implantable System 27

3.1.1 Forward Link Operation 27
3.1.2 Reverse Link Operation 31
3.2 Aging Test of the Implantable System 34
3.2.1 Electrode Array 35
3.2.2 Bioelectronic Implant 38
3.3 Bench-Top Test of the Biomimetic Stimulation System 40
Chapter 4 Pre-Clinical Trial: Intestinal Stimulation for Facilitating Gastrointestinal Motility 45
4.1 Background 45
4.2 Electrode Characterization 48
4.3 Stimulation-Parameter Identification in *In-Vivo* Acute Experiments 50
4.4 System Bench-Top Test 52
4.5 Preliminary *In-Vivo* Chronic Experiments 54
Chapter 5 Pre-Clinical Trial: Epidural Stimulation for Motor Function Recovery for the Spinal Cord Injured 58
5.1 Background 58
5.2 *In-Vivo* Acute Experiment: Selective Muscle Activation Using Implantable System 61
5.3 *In-Vivo* Acute Experiment: EMG-Mimetic Stimulation Using Biomimetic Stimulation System 64
Chapter 6 Conclusion and Future Work 68
Reference 71

List of Figures

Figure 1. Block diagram of the proposed implantable system for closed-loop neuromodulation. 5

Figure 2. Detailed block diagram of the SoC. 7

Figure 3. Chip micrograph of the SoC. 7

Figure 4. Concept illustration of biomimetic stimulation supported by the SoC. (a) An artificial signal resembling neural spike. (b) Command to trigger stimulation channel 1 and the induced stimulation output mimicking neural spike. (c) Commands to trigger stimulation channel 1 and channel 2 and the combined stimulation output mimicking neural spike. 9

Figure 5. Illustration of the heterogeneous packaging for the miniaturized bioelectronic implant. 11

Figure 6. Photo of the thin-film polyimide substrate. 11

Figure 7. (a) Photo of the implant prototype. (b) Zoom-in view of the SoC part in the implant under the microscope. 12

Figure 8. Functional block diagram of the rendezvous device. 13

Figure 9. Illustration of the operation of the DPSK transmitter. (a) Detailed block diagram of the DPSK modulator. (b) Waveforms of signal points in the block diagram. The representative data input is 4'b0100 and the data rate is 2 Mbps. 14

Figure 10. Illustration of the operation of LSK receiver. (a) Block diagram for illustration. (b) Waveforms of signal points in the block diagram. 16
Figure 11. Photo and the illustration of the prototype of the rendezvous device. 18
Figure 12. (a) Housing box design using SketchUp 3D modeling software. (b) Rendezvous device housed by the housing box..... 19
Figure 13. Conceptual diagram demonstrating applications of the biomimetic stimulation system. 21
Figure 14. Functional block diagram of the biomimetic stimulation system. 23
Figure 15. The logic flow diagram shows the sequence of control logic distributed between three main modules of the system. 24
Figure 16. The physical implementation of the portable biomimetic stimulation system.26
Figure 17. Bench-top test setup for forward link operation..... 28
Figure 18. Waveforms generated by the rendezvous device on the bench-top. 28
Figure 19. Waveforms of forward link operation on the bench-top. (a) System block diagram. (b) Power signal on the implant side. (c) The command transmitted by the rendezvous device (green trace) and command demodulated by the implant (yellow trace). (d) The command transmitted by the rendezvous device (green trace) and stimulation waveform (pink trace). (e) Zoom-in view of (d)..... 29
Figure 20. Demonstration of charge cancellation function. (a) Charge cancellation is OFF. (b) Charge cancellation is ON. 30
Figure 21. Bench-top test setup for reverse link operation..... 31

Figure 22. Measured results of the reverse link test. (a) Simulated EMG fed into the ADC input (signal point B in Figure 21); (b) zoom-in view of (a); (c) example waveform demonstrating the function of LSK transceiver. Blue trace is the output of LSK receiver (signal point F in Figure 21) while pink trace is waveform on the secondary side coil (signal point D in Figure 21); (d) another example waveform demonstrating the function of LSK transceiver. Yellow trace, blue trace, and pink trace are the input of LSK transmitter (signal point C in Figure 21), waveform on the primary side coil (signal point E in Figure 21), and output of LSK receiver (signal point F in Figure 21), respectively; (e) Reconstructed EMG signal on the GUI (signal point G in Figure 21); (f) zoom-in view of (e). 32

Figure 23. (a) Integrated power of the transmitted and reconstructed EMG bursts. (b) Regression plot of the integrated power of the transmitted and reconstructed EMG bursts. 33

Figure 24. Setup of the accelerated aging test. (a) The oven inside provides a constant temperature environment. (b) Oven outside. 37

Figure 25. (a)-(b) Side view and top view photo of the sealed glass bottle along with the electrode array. (c) Photo of the custom-designed lid. 37

Figure 26. Measured EIS result of the electrode array in the accelerated aging test. 38

Figure 27. Setup of the aging test for the bioelectronic implant. 39

Figure 28. The measured waveform of the bioelectronic implant under the aging test.... 40

Figure 29. (a) Measured multi-channel simulation with random IPI following exponential random distribution. Each stimulation channel has a mean IPI of 30 ms and an

output current of 500 µA. (b) Magnified view shows the different pulse widths and start delays among different channels. 42

Figure 30. Bench-top demonstration of multi-channel biomimetic waveform stimulation mimicking a recorded EMG waveform, which has been shown to be effective in epidural spinal cord stimulation for restoring motor function [9, 14]. (a) Desired biomimetic stimulation waveform. (b) The output of the prototype stimulator captured with an oscilloscope. 43

Figure 31. A continuous biomimetic current waveform is achieved by combining multiple channels together into a single output. 44

Figure 32. Illustration of using the developed wireless implant system for intestinal stimulation 48

Figure 33. Measured cyclic voltammogram of the electrode array in saline and intestinal fluid. 50

Figure 34. The measured weight of the expelled gel. (a) Results of individual pigs. (b) Averaged results 52

Figure 35. The 100 Hz, 2 mA, and 2 ms stimulus was generated by the wireless implant system on the bench-top. The cyan, pink, and blue traces are the command sent from the MCU in the RD, command demodulated by the DPSK receiver in the implant, and the induced output voltage waveform, respectively. The traces are presented in a time period of (a) 40 ms and (b) 10 ms. 53

Figure 36. Intestinal transit examined through X-ray photography. Pigs 1 and 2 are the control group, while 3 and 4 are the experimental group. (a) Fifteen metal beads were inside the intestine, and X-ray contrast was in the pigs' stomach

right after the surgery. (b) On postoperative Day 1, the contrast appeared in the rectum in Pig 4 with electrical stimulation, while the contrast had only moved to the intestines in other pigs, suggesting that electrical stimulation likely facilitates intestinal transit. The defecation of feces was also observable in Pig 4 but not in other pigs. (c) Contrast moved to the rectum in all pigs on postoperative Day 2. 56

Figure 37. Intestinal-tissue histology. (a) Normal jejunum distal to the surgical site (section 1), (b) jejunum that was attached to planar electrode array but did not receive stimulation (section 2), and (c) jejunum that was attached to planar electrode array and received stimulation (section 3). 57

Figure 38. Conceptual illustration of the implantable system for motor function recovery using a rat model [54]. 60

Figure 39. One stimulation event monitored by the oscilloscope. 62

Figure 40. Stimulation setting with a calibrated representation of the electrode array width and the distance between dorsal roots and the representative recorded single EMG. (a) Stimulation was delivered from rostral to caudal. (b) Stimulation was delivered from caudal to rostral. 64

Figure 41. Illustration of the experimental setup of EMG-mimetic stimulation. Adapted from [14]. 65

Figure 42. Stimulation setting with a calibrated representation of the electrode array width and the distance between dorsal roots. Adapted from [14]..... 66

Figure 43. (a) Recorded EMG waveform. The zoom-in view shows the representative EMG before and after EMG-mimetic stimulation. (b) The amplitude of each recorded EMG during the protocol. 67

List of Tables

Table I. Summary of measured electrochemical properties of electrode–intestinal fluid and electrode–saline interface. 50

Acknowledgment

I would like to express my sincere gratitude to my advisor Dr. Wentai Liu for the continuous support of my Ph.D. study. His guidance helped me in all the time of research and writing of this dissertation. His enthusiasm for knowledge and innovation always inspires me, even during tough times in the Ph.D. pursuit.

I would like to show my sincere appreciation to the rest of my dissertation and oral defense committee: Dr. Daniel T. Kamei, Dr. Eric Pei-Yu Chiou, and Dr. Hsian-Rong Tseng for their insightful comments and encouragement.

I would like to acknowledge the financial support of this dissertation research - NIH BRP U01 EB007615 and NSF SBIR 1647917.

I would also like to thank my group members: my senior Dr. Yi-Kai Lo for his supervise and assistance; my colleagues Stanislav Culaclii, Yushan Wang, and Yan-Peng Chen for their support and discussion; and other members including Dr. Chihwei Chang, Dr. Ying Li, Dr. Ming-Dao Wu, Hanyue Zhou, Jonathan Massachi, William Yang, Benjamin Wood, Zhaohao Mai, Zhaoyi Liu, Michael Chan, Yan Long, Smiti Narayanan, Brett Bailey, Jia-Heng Chang, En-Lin Hsiang, and Luyao Chen for their help.

My appreciation also goes to the collaborators: Dr. Reggie Edgerton and Dr. Giuliano Taccola for the support in rat experiments, especially Dr. Taccola for the data analysis; and Dr. James Dunn, and Genia Dubrovsky for the support in pig experiments.

I would like to express my deepest gratitude to my parents, my younger brother, my parents in law, and my older brother in law for their timely and selfless support. Most

importantly, this dissertation would not have been possible without the endless love and unconditional support from my beloved wife.

Biographical Sketch

Po-Min Wang received the B.S. and M.S. degrees in Dept. of Electrical Engineering from National Tsing Hua University, Hsinchu, Taiwan, in 2008 and 2011, respectively.

From 2009 to 2011, he interned with National Chip Implementation Center (CIC), Hsinchu, Taiwan, and worked on the measurement of RF circuits and systems. In March 2011, he joined Mstar Semiconductor, Hsinchu, Taiwan, where he designed RF frequency synthesizers for wireless cellular applications. From 2012 to 2015, he worked in MediaTek Inc., Hsinchu, Taiwan, where he developed RF frequency synthesizers and mixed-signal baseband PLLs for wireless connectivity SoCs as an RF/mixed-signal IC engineer.

He began his pursuit of a Ph.D. degree in Dept. of Bioengineering, University of California, Los Angeles in 2015. He received the Graduate Division Fellowship in 2018.

Chapter 1
Introduction

Neuromodulation is an emerging and promising method to treat diseases that are incurable by pharmaceutical means. Unlike pharmaceutical agents whose target are molecules, neuromodulation restores the dysfunctional biological systems by modulating proper nervous systems. Among various neuromodulation approaches, functional electrical stimulation has been widely adopted for various applications. Well-known examples include spinal cord implant for pain relief [1], gastric stimulation for the treatment of digestive disease [2], and vagus nerve stimulation for weight control [3]. Those neuromodulation devices adopt a conventional modulation scheme in which electrical stimulation is delivered in an open-loop fashion and electrical pulses are in a regular and periodic pattern.

With advances in neuroscience, technological advancement for neuromodulation devices is essential in order to support emerging applications that require sophisticated neuromodulation scheme. In recent years, the idea of electroceuticals has been advocated by several pharmaceutical companies as well as U.S. government agencies including National Institutes of Health (NIH) and Defense Advanced Research Projects Agency (DARPA) [4-6]. In contrast to conventional neuromodulation that only requires open-loop modulation, electroceuticals need to dynamically adjust the stimulation protocol in response to the subject's physiological state, thus requiring a physiological response recording system as well as an adaptive control algorithm in order to achieve closed-loop

neuromodulation. In addition to electroceuticals, some other applications also need to deliver the stimulation in a closed-loop fashion, e.g. brain-machine interface (BMI) [7] and spinal cord stimulation for motor function recovery after spinal cord injury [8]. Both BMI and spinal implant need to record biological signals (i.e. brain signals and electromyography signals) real-time and adjust the stimulation parameter accordingly to activate the targeted muscles. Another promising neuromodulation scheme is biomimetic stimulation. It has been demonstrated that non-periodic, non-uniform pattern that mimics biological signals achieves more effective neuromodulation in some applications. For example, in the epidural stimulation for restoring motor functions, a stimulus pattern mimicking a pre-recorded electromyography (EMG) signal is more effective in activating spinal cord locomotion circuits compared to the uniformly periodic protocol [9]. In addition, neuromodulation using non-regularly timed stimuli for deep brain stimulation has produced better therapeutic effects for treating Parkinson's [10]. Finally, stimuli timed with a random exponential distribution that mimics the random neural spikes prevent adaptation of retinal ganglion cells, promising to reduce undesired image "fading" effect in retinal prostheses [11].

Despite increasing interests in closed-loop neuromodulation and biomimetic stimulation, existing implantable neuromodulation devices have limited capability in supporting those sophisticated modulation schemes. The state of the art device targeting BMI currently supports 3,072 channels of stimulation and recording [12]. Yet the closed-loop capability, as well as the implantability of the device, have not been demonstrated. The work only reported the results of brain recording through wire connection while the test of stimulation, wireless powering, and wireless data communication was missing.

Recently, a human clinical study of closed-loop epidural stimulation for motor function recovery has been presented [13]. The closed-loop neuromodulation was achieved by the non-invasive recording of the EMG and inertia and then triggering the desired stimulation protocol pre-loaded in an implantable spinal stimulator accordingly. However, the stimulator only supports the periodic and regular stimulation pattern with limited programmability. This limitation impedes the usage of stimulator to explore the complex working mechanism of spinal network and to generate a more effective stimulation patterns for epidural stimulation, e.g. EMG pattern for lowering the activation threshold of the motor neurons [14] and kHz stimulation for mitigating the undesired paresthesia [15].

This dissertation presents the design of wireless biomimetic circuits and systems aiming to fill the technology gap. Two systems are designed and reported in Chapter 2: 1) An implantable stimulation and recording system for closed-loop neuromodulation; 2) A biomimetic stimulation system. The validation of both systems on bench-top is provided in Chapter 3. Physiological experiments using both systems are also demonstrated: Chapter 4 presents intestinal stimulation for facilitating gastrointestinal motility in porcine models while Chapter 5 presents epidural stimulation for recovering motor functions for the spinal cord injury in rat models. Chapter 6 draws the conclusion and future work.

Chapter 2
Design of Wireless Biomimetic Circuits and Systems

2.1 IMPLANTABLE STIMULATION AND RECORDING SYSTEM

2.1.1 System Overview

Considering implantability, device miniaturization, and capabilities of biomimetic stimulation and closed-loop control, the system architecture is designed as shown in Figure 1. The proposed system consists of a miniaturized bioelectronic implant, a custom-made graphical user interface (GUI) on a tablet for configuring the implant, and a rendezvous device (RD). The RD carried by the subject receives user-defined commands from the GUI via the WiFi link and delivers power and command to configure the implant through inductive links. This two-level wireless transmission scheme allows remote control of the system in meter range while delivering power and command to the implant inside the body with acceptable signal attenuation.

The core of the implant is a versatile system on a chip (SoC) that supports wireless power and bi-directional data transfer via inductive links, and multi-channel biomimetic stimulation and recording. The wireless powering enables the implant of the system while avoiding the use of a bulky rechargeable battery in the implant. The bi-directional data transfer allows real-time updates of stimulation parameters through forward link (from the external side to the implant side) while wireless recording through reverse link (from the implant side to the external side), achieving a closed-loop

operation. Note that the closed-loop control algorithm is implemented at the external side instead of on the SoC for flexibility and expandability. As the optimal control algorithm varies with different applications, this flexibility enables researchers to update the algorithm tailored for various needs. On the other hand, the on-chip biomimetic stimulation controller enables the generation of versatile stimulation pattern including regular pulses and biomimetic waveforms. All the above-mentioned functions are integrated into a miniaturized SoC. The SoC is integrated with a thin-film electrode array into an implant with a small form factor via a heterogeneous packaging approach. The implant is then encapsulated by biocompatible epoxy for chronic implantation.

This dissertation focuses on the development of the hardware part of the system. The following subsections present the design of a miniaturized bioelectronic implant and rendezvous device.

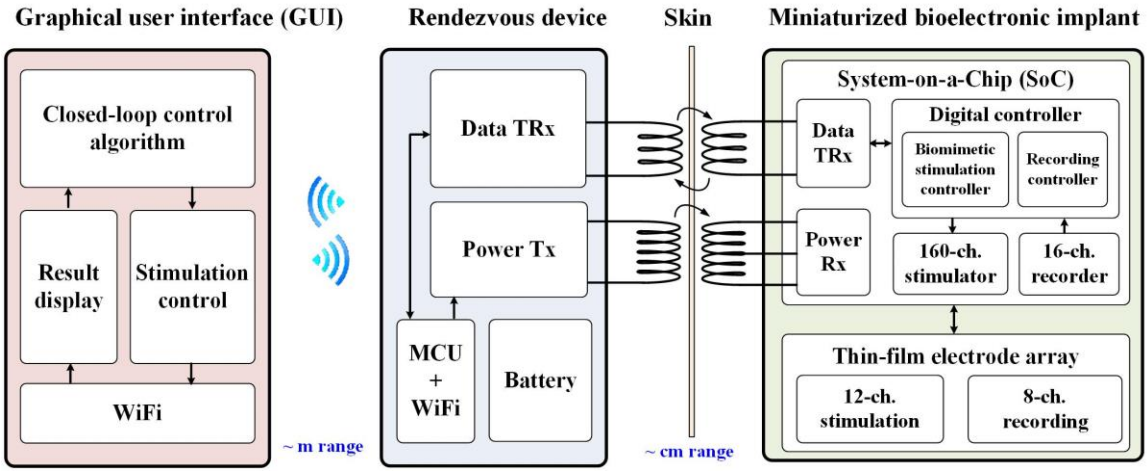

Figure 1. Block diagram of the proposed implantable system for closed-loop neuromodulation.

2.1.2 Miniaturized Bioelectronic Implant

The design of the miniaturized bioelectronic implant is divided into two subsections: 1) system on a chip (SoC), and 2) thin-film electrode array and heterogeneous system integration.

2.1.2.1 System on a Chip (SoC)

A detailed block diagram of the custom-designed SoC is shown in Figure 2 [16] with a chip micrograph shown in Figure 3. The SoC is designed and fabricated with TSMC 0.18 μm 32 V HV 1P6M CMOS process. The quad-voltage power converter consisting of rectifiers and voltage regulators receives inductive power signals from the rendezvous device (RD) and provides regulated ±1.8 V to supply the data transceiver and the control logic, and ±12 V to the current driver in the stimulator. The high compliance voltage for the stimulator is critical as it allows a wide range of parameters for current-mode stimulation. In the bi-directional data link, the forward link (from the external side to the implant side) and the reverse link (from the implant side to the external side) share the same coil with a low quality factor to achieve a high data rate [17]. A unique quasi full-duplex approach based on time multiplexing supports the bi-directional operation of the data link [16]. The data transceiver incorporates a differential phase-shift keying (DPSK) receiver for its good immunity to interference in amplitude domain and a load-shift keying (LSK) transmitter for low-power consumption. The DPSK receiver in the forward link demodulated the incoming signal sent by the DPSK transmitter in the RD back to the digital command issued by the user. The command is then decoded by the biomimetic stimulation controller, and the stimulator is set to accordingly generate the desired electrical stimuli. On the other hand, in the reverse link, the analog front-end and

analog-to-digital converter (ADC) amplifies and digitizes the recorded physiological signal into digital bitstreams. The bitstreams are serialized by the recording controller and then sent to the LSK transmitter. The LSK modulated physiological data is then transmitted to the external LSK receiver in the RD.

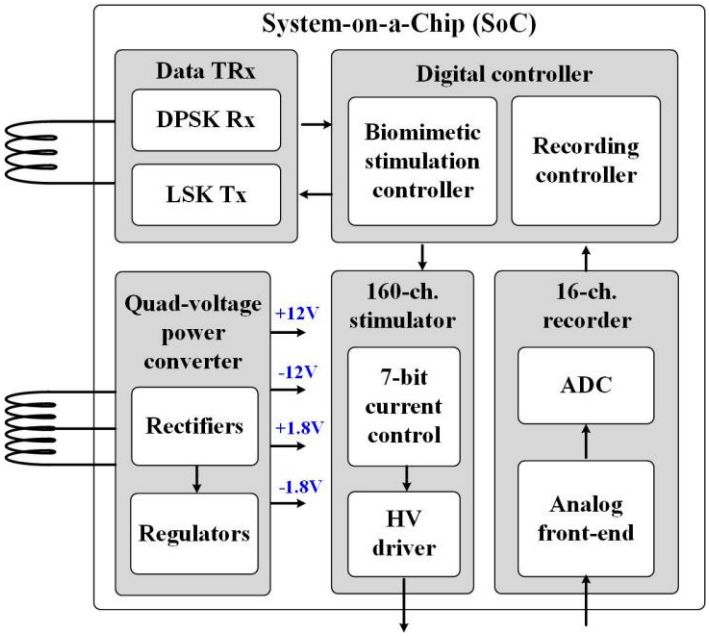

Figure 2. Detailed block diagram of the SoC.

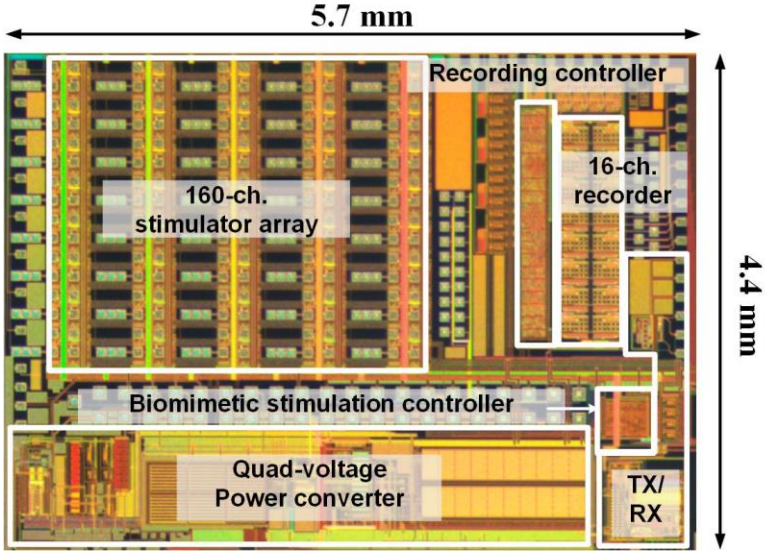

Figure 3. Chip micrograph of the SoC.

The biomimetic stimulation controller enables the stimulator to support a wide range of regular pulse with intensity from 0.3 μA to 0.5 mA, a pulse width from 10 μs to a user-defined length, and a frequency from 0.001 to 200 Hz. In addition to this high programmability for periodic pulses, the controller allows direct control of amplitude and width of each individual current pulse and their timing within the desired output waveform. This capability ultimately enables unique dynamic stimulation patterns such as random pulse periods and biomimetic waveform generation on multiple stimulation output channels. The working mechanism of the biomimetic stimulation supported by the SoC is illustrated in Figure 4. An artificial signal resembling a neural spike is used for illustration (Figure 4(a)). The biomimetic stimulator is able to produce individual pulses with desired amplitudes such that the stimulation waveform mimics the artificial neural spike (Figure 4(b)). Each pulse is generated by a command. A gap exists after each pulse, which is required by the command that configures the stimulation controller to generate the next pulse. Nevertheless, the gap can be eliminated by combining multiple stimulation channels with predetermined timing settings such that the gap in one channel is occupied by the current output of another. This achieves a continuous biomimetic waveform without gaps (Figure 4(c)).

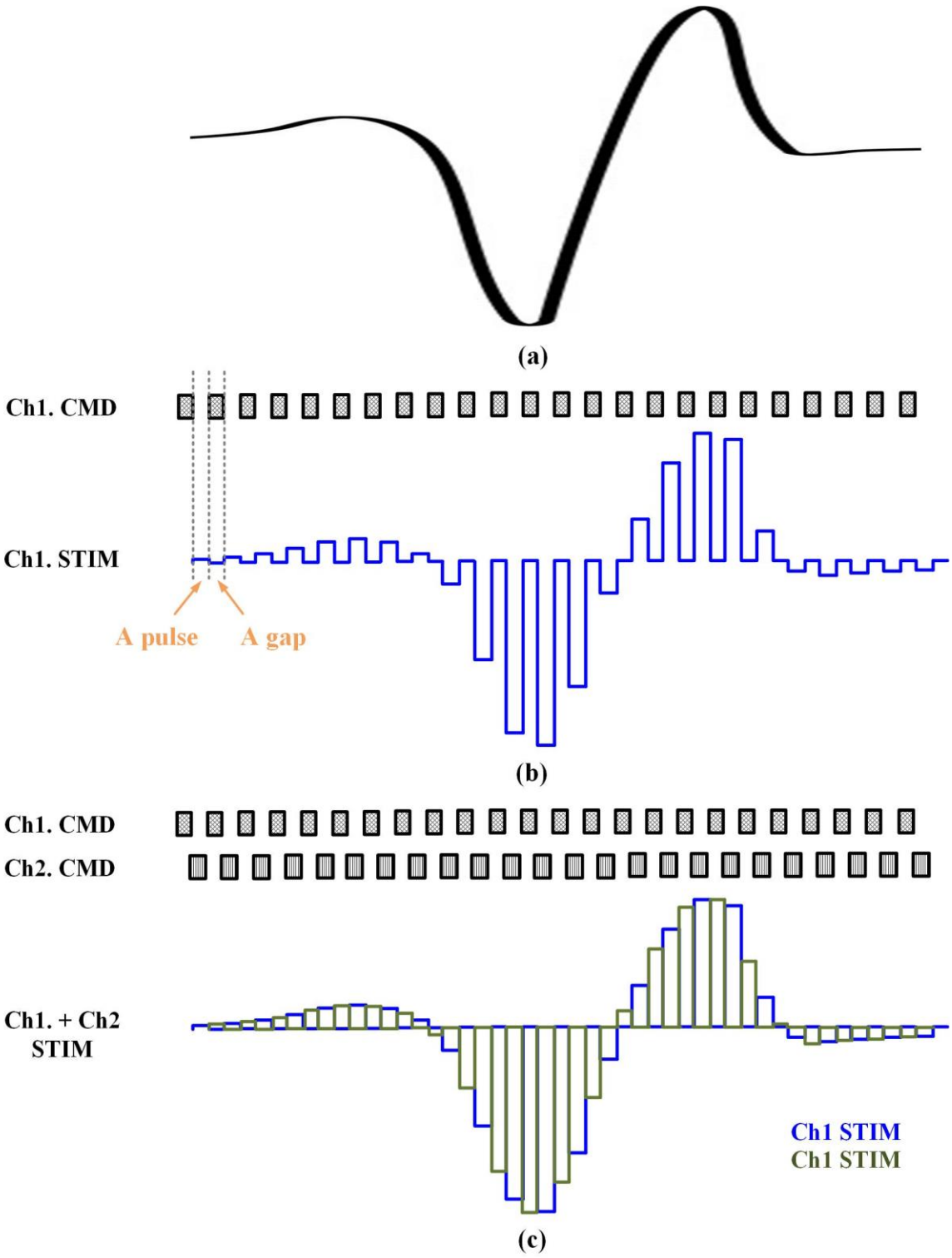

Figure 4. Concept illustration of biomimetic stimulation supported by the SoC. (a) An artificial signal resembling neural spike. (b) Command to trigger stimulation channel 1 and the induced stimulation output mimicking neural spike. (c) Commands to trigger stimulation channel 1 and channel 2 and the combined stimulation output mimicking neural spike.

2.1.2.2 Thin-Film Electrode Array and Heterogeneous Packaging

The heterogeneous packaging technique utilizes an 8 μm-thick thin-film polyimide-based substrate to integrate the SoC, printed-circuit board (PCB), off-chip components, and electrode array into a miniaturized bioelectronic implant (Figure 5) [18]. The polyimide substrate serves as not only the electrode array for stimulation and recording but also a flexible circuit board that achieves all required electrical connections in the implant. The electrodes, bond pads, and the interconnections on the substrate are made of platinum/titanium (200 nm/10 nm thickness) fabricated by the e-beam evaporated deposition technique developed in our laboratory [19]. All required electrical connections for enabling system function (e.g. the connection between electrodes and outputs of stimulation drivers) are achieved by the patterned metal trace on the polyimide substrate as well as the gold bumps and ball-bonded gold wires. The gold bumps connect the polyimide substrate with the SoC while the connection among the substrate, SoC, and the PCB are made by the ball-bonded gold wires. The use of a small footprint PCB significantly facilitates the development of implant prototype. This configuration enables the design debugging, and the monitoring of critical signals in the SoC through directly probing PCB pads during the system bench-top test. Nevertheless, it should be noted that the PCB is not a necessary part in the final implant design. Indeed all off-chip components can be connected to pads on the polyimide substrate via the silver conductive paste in the absence of PCB. After the assembly process, the implant is encapsulated by the epoxy (3M DP100 Plus Clear, 3M Corp., Maplewood, MN). The materials interface with the biological tissue including the polyimide, platinum, and epoxy are all biocompatible.

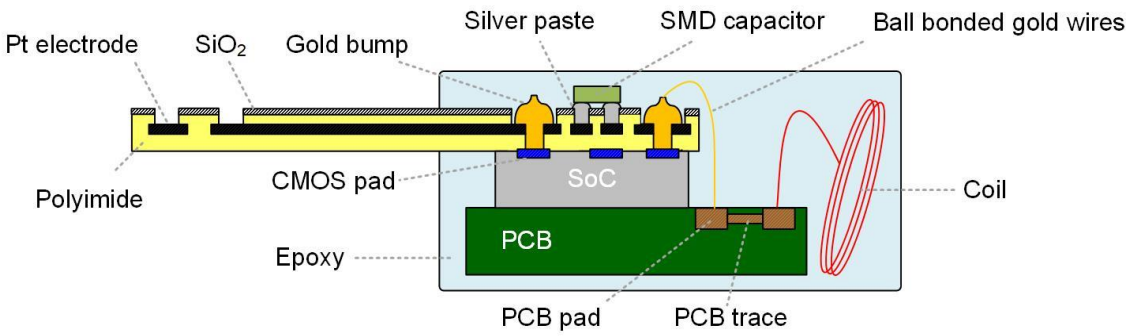

Figure 5. Illustration of the heterogeneous packaging for the miniaturized bioelectronic implant.

Figure 6 shows the photo of the thin-film polyimide substrate while Figure 7 shows the prototype of the miniaturized bioelectronic implant. In Figure 7, the power and data coils are arranged coaxially, which reduces the size of the implant. The separation between the coils and the PCB can be adjusted for different applications. For example, this prototype was used for the intestinal stimulation in porcine models, as presented in Chapter 4, and this configuration was suggested by the surgeon in favor of device implantation during the surgical procedure. This implant tailored for GI stimulation has a weight of ~4.2 g and a volume of ~4.9 cm^3, which is at least an order lighter and 7.7 times smaller than existing commercialized GI implantable stimulators [20, 21].

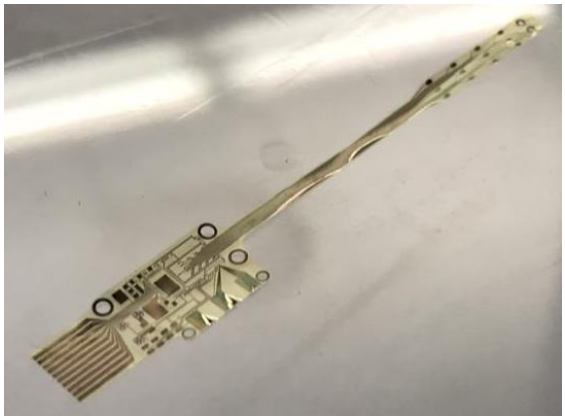

Figure 6. Photo of the thin-film polyimide substrate.

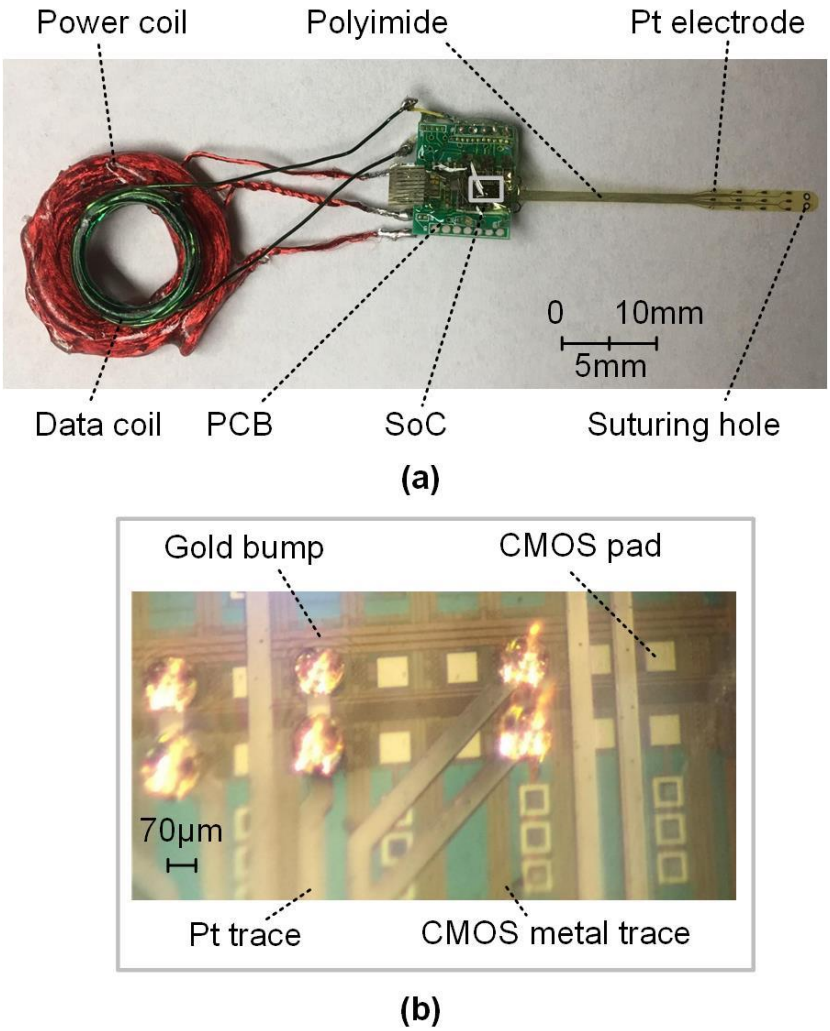

Figure 7. (a) Photo of the implant prototype. (b) Zoom-in view of the SoC part in the implant under the microscope.

2.1.3 Rendezvous Device

The rendezvous device (RD) made by off-the-shelf components receives the command from the GUI on the tablet via WiFi and accordingly powers and configures the miniaturized implant through dual-band inductive telemetries (Figure 8). The carrier frequencies of the power and data links are 2 MHz and 22 MHz, respectively. This one decade away frequency separation allows the use of signal filtering in the DPSK receiver to relieve the power to data interference. In the power transmitter, a high-efficient class-E

power amplifier is designed to drive the primary side power coil [22]. The power amplifier is supplied by an adjustable regulator with a voltage ranged from 2 to 10 V. This adjustability enables the power transmitter to tune the output power level based on the variation of coupling coefficients between the coil pairs in order to optimize the power transfer efficiency, i.e. closed-loop power adjustment.

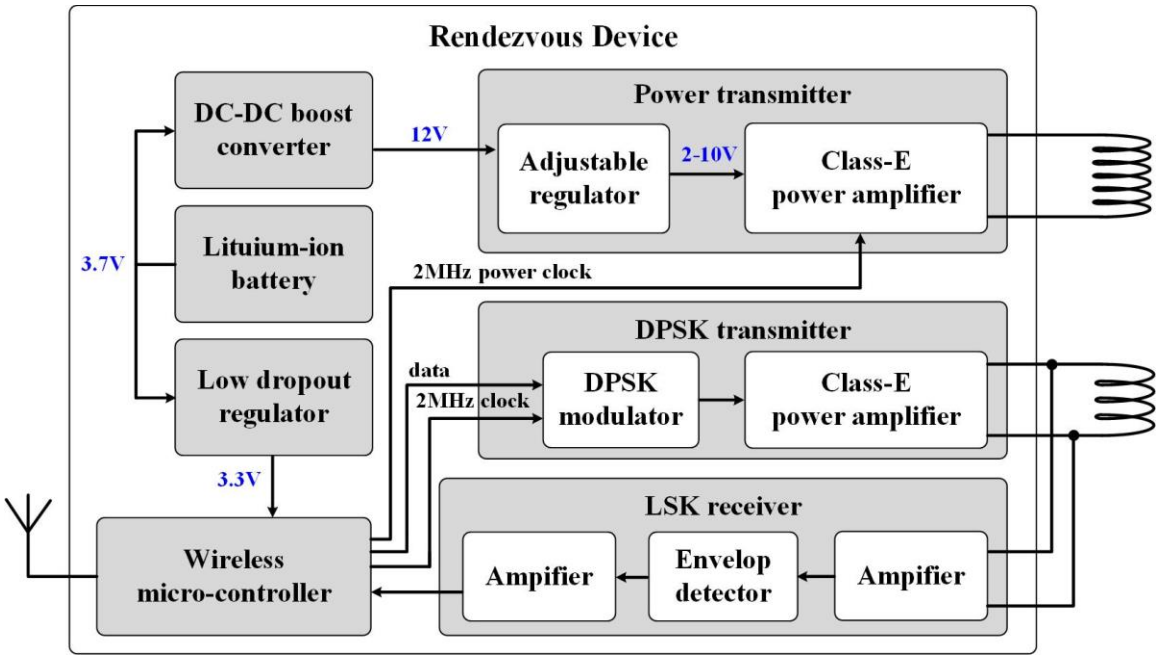

Figure 8. Functional block diagram of the rendezvous device.

In the DPSK transmitter in the forward data link, the same architecture of the class-E power amplifier is used, and the amplifier is driven by a non-coherent DPSK modulator [23]. This modulation scheme encodes the command bit in the relative phase shift between two consecutive symbols rather than the phase shift to a reference clock, which avoids a complicated synchronization circuit in the implant side, e.g. phase-locked loop. The scheme is realized by the XOR gate, D flip-flop, multiplexer, 22 MHz crystal oscillator, and inverter (Figure 9). The 22 MHz crystal oscillator along with the inverter generates two “out of phase” 22 MHz sinusoidal carrier signals (waveform E and F in

Figure 9). Because of the operation of the XOR gate, the D flip-flop toggles when the input bit is logic one and remains unchanged when the input bit is logic zero. The toggling of D flip-flop changes the phase of 22 MHz carrier that drives the class-E power amplifier, achieving DPSK operation (Figure 9).

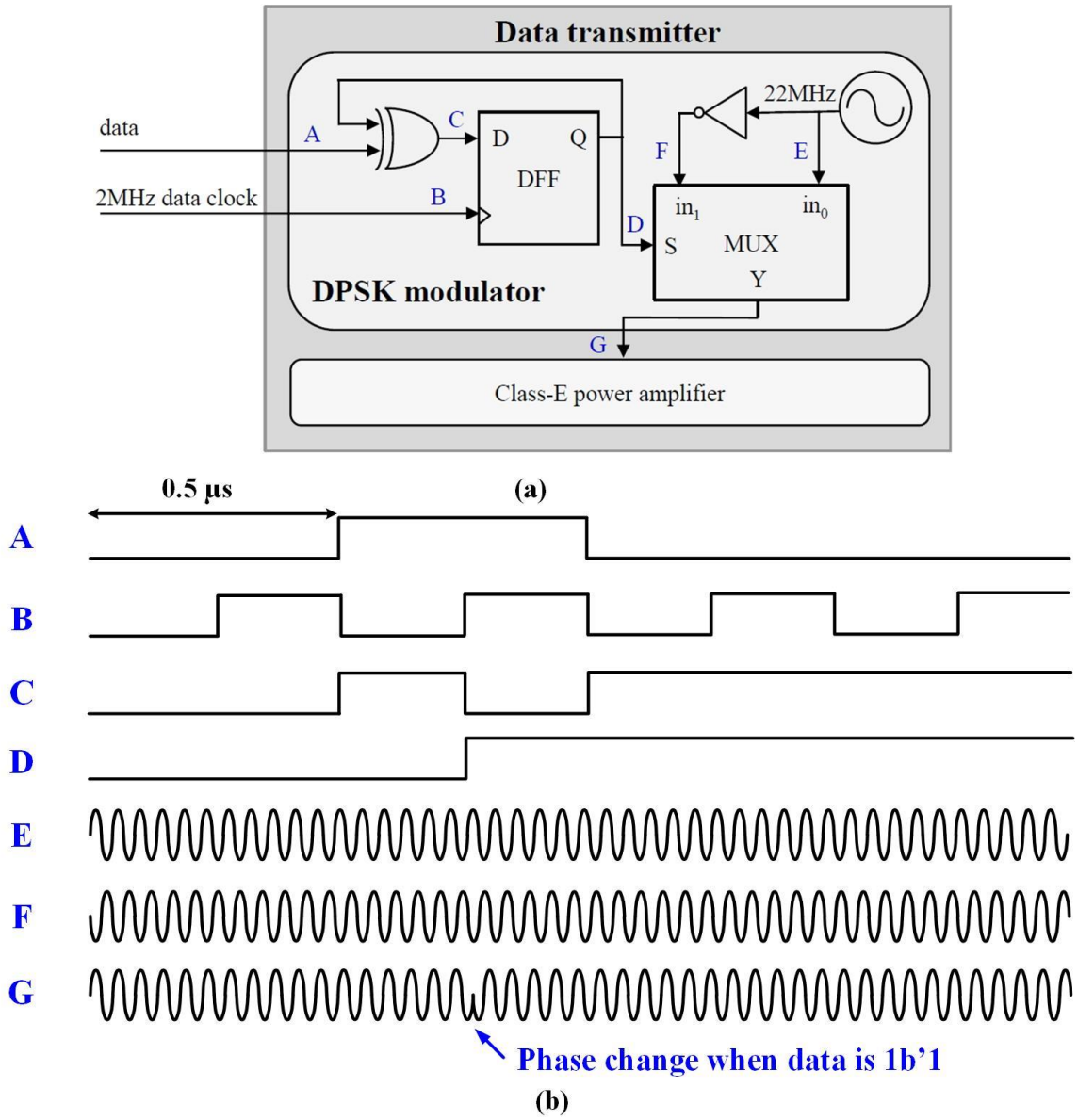

Figure 9. Illustration of the operation of the DPSK transmitter. (a) Detailed block diagram of the DPSK modulator. (b) Waveforms of signal points in the block diagram. The representative data input is 4'b0100 and the data rate is 2 Mbps.

On the other hand, in the reverse data link, an LSK receiver demodulates the LSK-modulated recorded signal back to digital bitstreams. The bitstreams are then transmitted to the micro-controller in the RD, which relays the bitstreams to the GUI through the WiFi link for signal reconstruction. The detailed operation principle of the LSK data link is illustrated in Figure 10. As an example, a digital bitstream of 4'b1011 with a data rate of 2 Mbps is used for illustration (waveform A in Figure 10). The LSK signal on the coil pair contains a 22 MHz carrier that is generated by the DPSK transmitter with a constant phase, i.e. no toggling of D flip-flop in DPSK modulator. On the implant side, the amplitude of the carrier is modulated by the NMOS switch in the LSK modulator, such that the amplitude is zero when input is 1'b1 and remains unchanged when input is 1'b0 (waveform B in Figure 10). Because of the nature of mutual inductance, the amplitude of the carrier on the external side coil is reversed (waveform C in Figure 10). The received LSK signal is then amplified and its enveloped is extracted by an envelope detector. The pole in the enveloped detector is properly designed such that the 22 MHz carrier is significantly attenuated while the 2 Mbps data transition is mostly preserved (waveform D in Figure 10). The envelope extracted signal is finally amplified to a rail-to-rail signal that is identical to the transmitted digital bitstreams (waveform E in Figure 10).

The clocks and data command required by the power and data transmitters are generated by a micro-controller (CC3200, Texas Instruments, Dallas, TX) that can be wirelessly controlled by the tablet through WiFi (Figure 8). With a 3.7 V lithium-ion rechargeable battery, the DC-DC converter and low dropout regulators provide the

regulated power to the circuits in the RD. The wireless and battery power features allow the RD to be carried by the freely moving subjects receiving the implant.

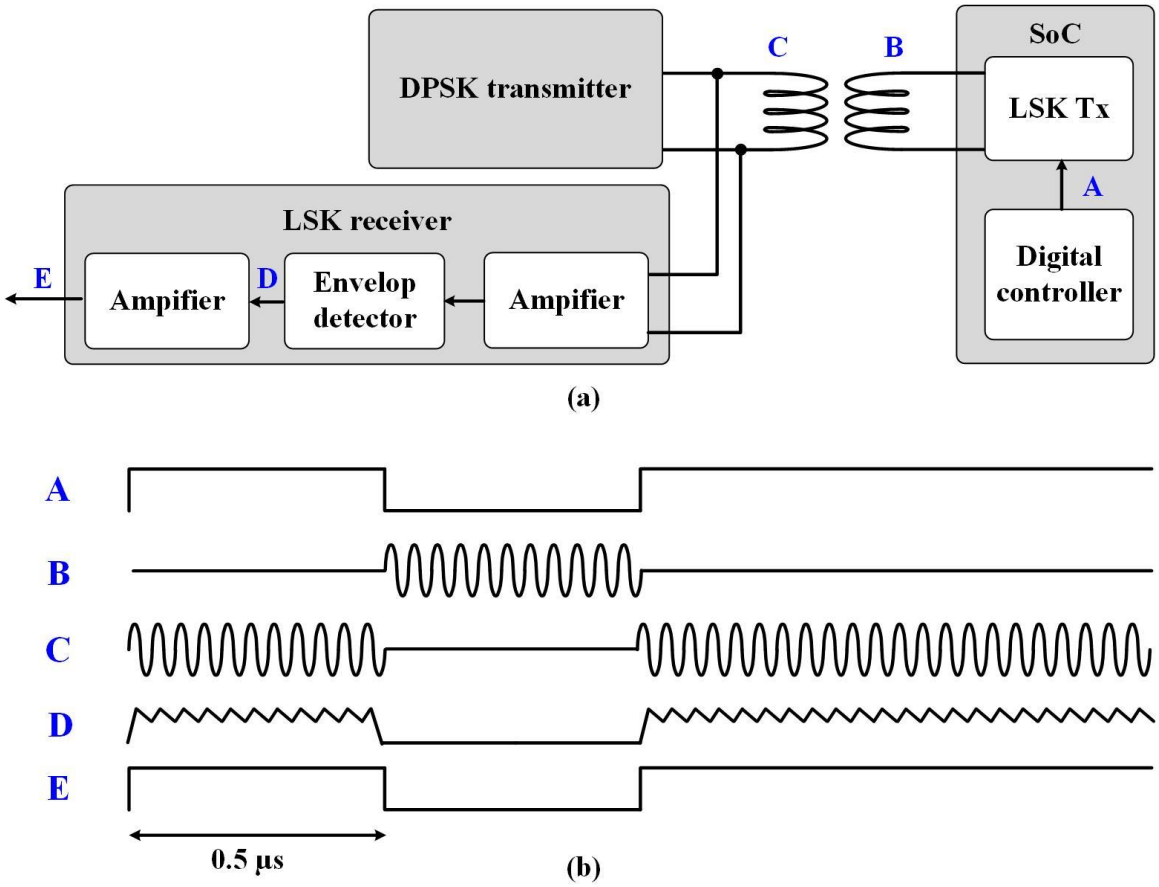

Figure 10. Illustration of the operation of LSK receiver. (a) Block diagram for illustration. (b) Waveforms of signal points in the block diagram.

The photo and the illustration of the RD prototype are shown in Figure 11. The RD is partitioned into four pieces: 1) micro-controller (MCU) board, 2) data transmission board that contains DPSK transmitter and LSK receiver, 3) power transmission board that contains power transmitter, DC-DC boost converter, and low dropout regulator, and 4) rechargeable battery. The three boards are stacked together via the board to board connectors. This stacked-board design offers several advantages: 1) the signal to noise

ratio of noise-sensitive circuit blocks can be improved through proper deployment of circuitries. For example, the MCU that contains the WiFi link and the power transmitter are arranged on different boards so that the strong power interference from the power transmitter to the sensitive WiFi RF signal is reduced. 2) The space usage of this design is superior to the design that has all circuits on a single board. 3) The weight of this design is lighter than the single board design, as the thickness of each board can be optimized individually. In order to achieve a 50 Ω RF matching for the antenna in the WiFi link, the MCU needs to use a 1.1 mm-thick board which is suggested by the manufacturer. However, both power transmitter and data transceiver do not have this limitation. It is thus feasible to use a 0.4 mm-thick board for the power transmitter and data transceiver to reduce the weight. By doing so, the weight of the design is reduced by 22.6%.

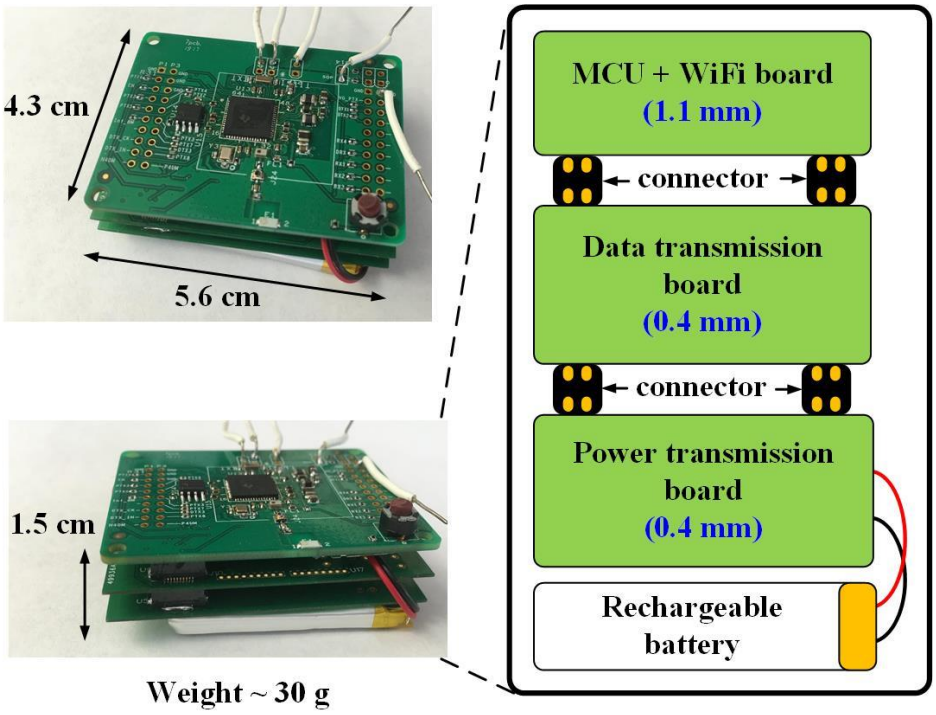

Figure 11. Photo and the illustration of the prototype of the rendezvous device.

A box for housing the RD that consists of the three boards, battery, and coils was designed and 3D-printed (Figure 12). The box integrated different components into one piece, which simplifies the process of placing the RD in the pocket of the jacket worn by the subject. The RD prototype has a dimension of 5.8 cm × 4.5 cm × 4.8 cm and a total weight of 70 grams. This weight is acceptable for the pig that will carry the RD for chronic implantation, as presented in Chapter 4. It is possible to further shrink both the size and weight of the box for small subjects, e.g. rat.

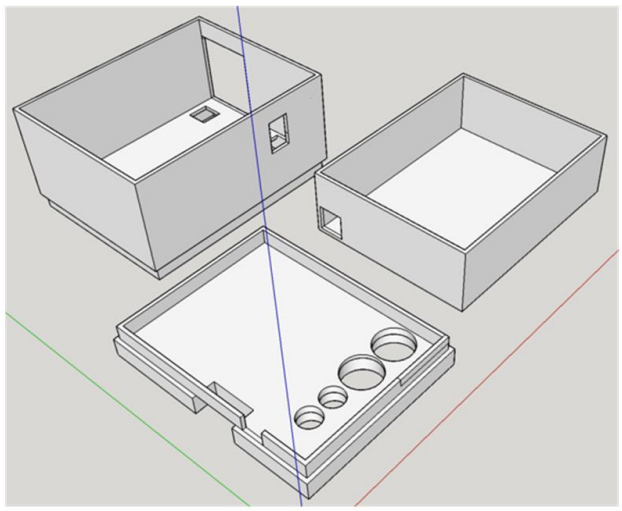

(a)

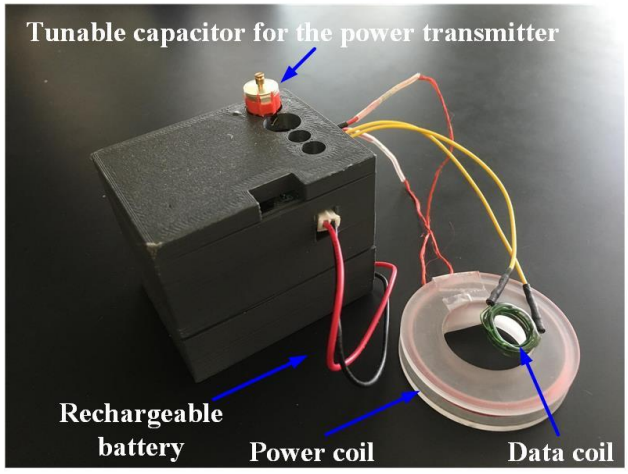

(b)

Figure 12. (a) Housing box design using SketchUp 3D modeling software. (b) Rendezvous device housed by the housing box.

2.2 BIOMIMETIC STIMULATION SYSTEM

2.2.1 Background

Biomimetic stimulation is a promising neuromodulation scheme that is shown to be more effective than the conventional regular and periodic pulse in several applications [9-11, 24]. However, as the therapeutic effect of this emerging approach on many other biomedical applications is still unclear, the investigation of various biomimetic

waveforms on the targeted application using an animal model is required. It is thus essential to have a biomimetic stimulation system suitable for the identification of stimulation parameters in acute animal experiments. Noted that the acute animal experiment does not need chronic implantation, it is thus feasible to use a non-implantable stimulation system to simplify the experimental setup.

Such a biomimetic stimulation system requires a sophisticated stimulator solution. The most common approaches use bulky stimulators which can mimic a preloaded waveform, e.g. computer with a data acquisition (DAQ) device [10] or desktop stimulator [25]. These commercial devices are not translatable to either implantable application or a responsive system that can adjust its stimulation based on the bio-recordings in real-time. A few implantable and programmable neural stimulators, demonstrated previously, can adjust their pulse widths and firing frequencies, or turn on or off based on external commands [26, 27]. Yet they lack the ability to adapt the amplitude of each stimulation parameter in real-time and are thus unable to mimic the biological signal waveforms.

The following subsections present the implementation of a biomimetic stimulation system aiming to provide a reliable platform for quick evaluation of biomimetic stimulation therapy on animal models. The core of the system is the wireless SoC presented in Subsection 2.1.2.1. Because of the versatility of the SoC, the biomimetic stimulation system is flexible to be advanced to an implantable, real-time closed-loop, bi-directional system for various applications (Figure 13).

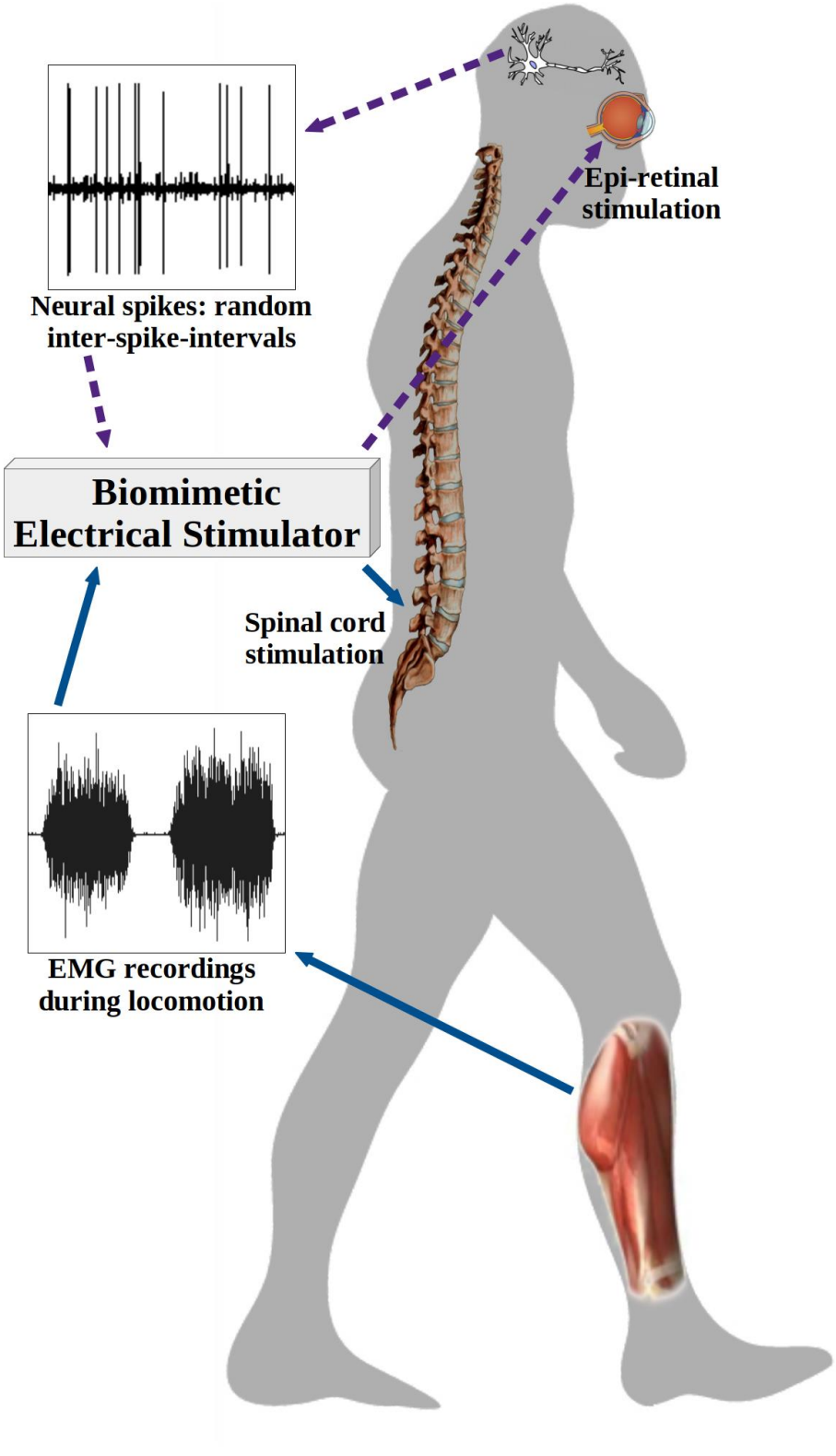

Figure 13. Conceptual diagram demonstrating applications of the biomimetic stimulation system.

2.2.2 System Overview

The biomimetic stimulation system is designed to support features of portability, single battery power, wireless user interface, user-defined arbitrary stimulation patterns, and concurrent multi-channel stimulation [28]. The functional block diagram of this system is shown in Figure 14. The core of the stimulator is our custom-developed wireless SoC. The clock and commands required by the SoC for generating the stimulation output are sent from a control unit via wire connection. The level shifter consisting of inverters in the control unit achieves voltage level translation between the micro-controller (logic one: 3.3 V; logic zero: 0 V) and the SoC (logic one: 0 V; logic zero: -1.8 V). The SoC notably also supports wireless power and data transmissions via telemetry coils, which allow the stimulation system to support implantable applications as needed. The control unit is then wirelessly configured by the graphical user interface (GUI) in a mobile device through a WiFi link. The GUI allows the researchers to define stimulation patterns tailored to the targeted biomedical application. The supply voltages of the SoC and the control unit are generated by a power supply unit whose power source is a single 3.7 V lithium-ion battery. The power supply unit is constructed by an off-the-shelf DC-to-DC converter and low dropout voltage regulators manufactured by Analog Devices (Norwood, MA). The DC-to-DC converter (ADP5070) generates ±15V simultaneously from the battery. The ±15 V are then translated to ±12 V to supply the SoC by ADP7142 and ADP7182 regulators, respectively. In order to ensure the symmetry between ±1.8 V, they are generated from ±12 V through other ADP7142 and ADP7182 regulators. The 3.3 V for the control unit is directly regulated from the battery by ADP7158 regulator to avoid extra power loss.

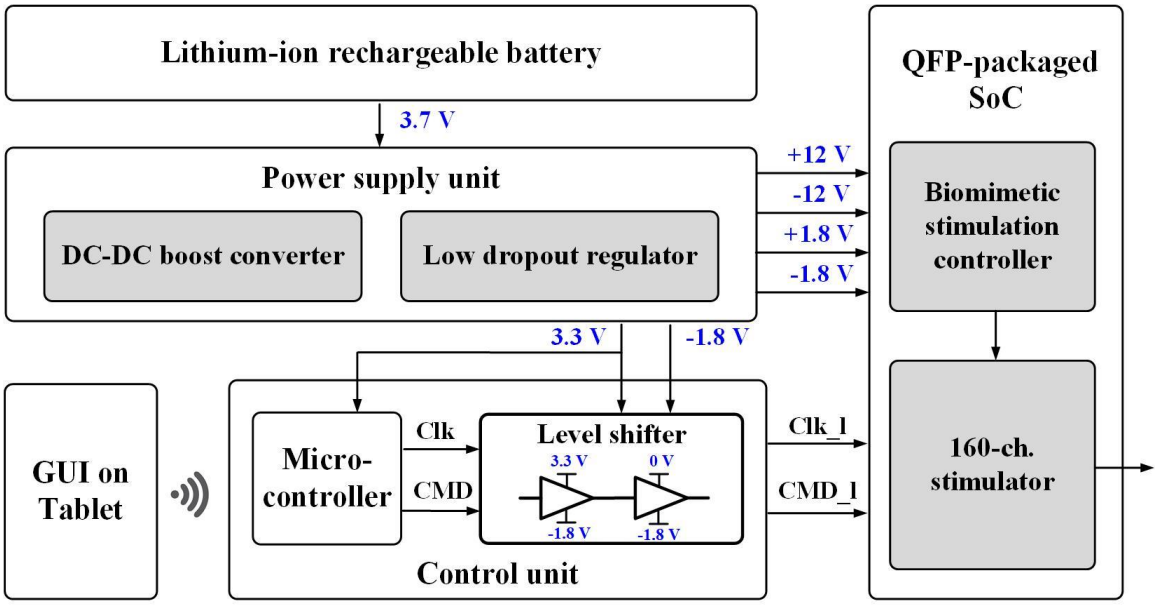

Figure 14. Functional block diagram of the biomimetic stimulation system.

It is worthy to note that this proposed system design not only achieves a highly flexible and compact stimulation-platform technology but also offers the flexibility of upgrading to the next generation real-time closed-loop system, which will include simultaneous recording and stimulation. For example, WiFi communication protocol is selected instead of Bluetooth because its high data rate can support more channels of wireless recording. In addition, the battery-powered scheme eliminates the potential 60 Hz noise issue, which increases signal fidelity in the recording circuitry.

2.2.3 Design and Implementation

The working mechanism of biomimetic stimulation supported by the SoC has been illustrated in subsection 2.1.2.1. In this subsection, the logic design of the complete stimulation system and the system implementation are presented. The control logic is distributed across three major components shown in Figure 15: the software app code in the GUI device, the firmware code executed by the microcontroller in the control unit,

and digital very-large-scale integration (VLSI) circuit in the SoC. The logic architecture places more computational demand on the former two components of the system while the least computational logic resides in the SoC's digital controller allowing it to have small size and power consumption, thus reducing invasiveness in implantable applications. This logic architecture generates a unique data packet in real-time in response to the required stimulation parameters for each individual stimulus instance.

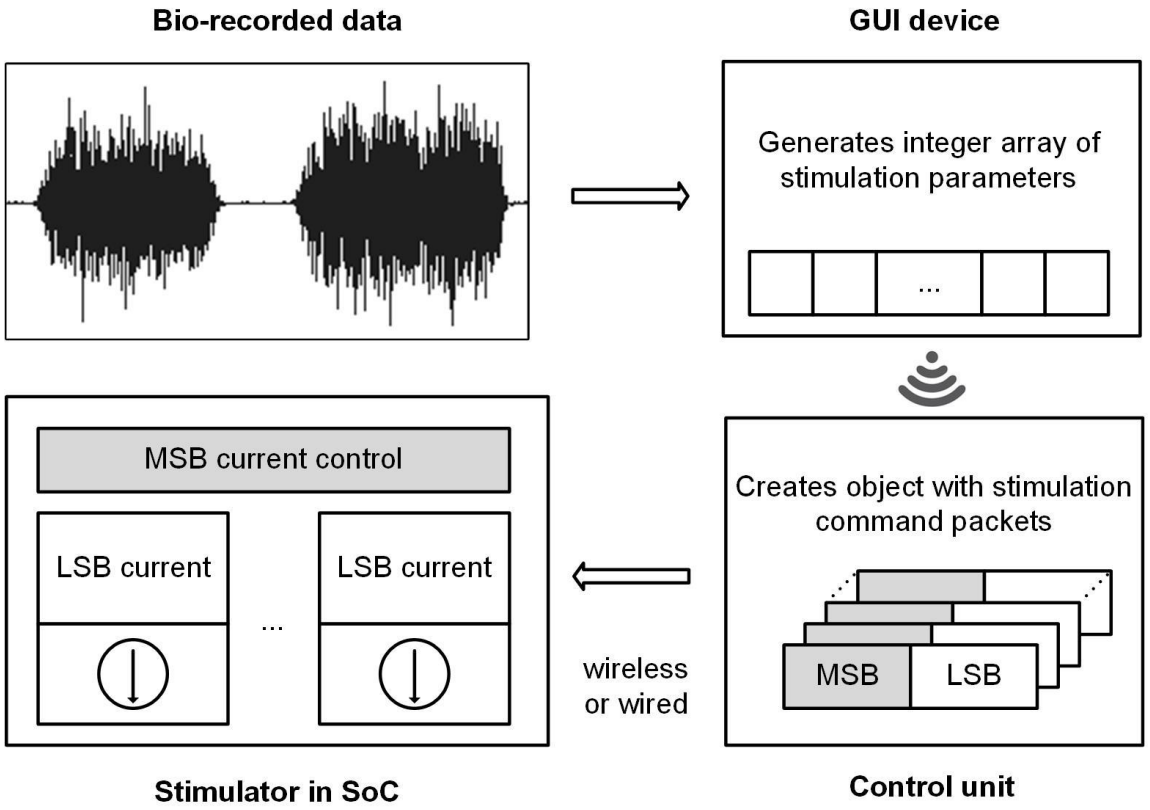

Figure 15. The logic flow diagram shows the sequence of control logic distributed between three main modules of the system.

When using the system for stimulating with a pre-recorded biomimetic signal, the GUI device is programmed by the user with a CSV file describing the desired signal waveform. This waveform is transferred as a set of integers to the control unit. The control unit constructs a full data packet from integers for each data point, where the data

packet defines the stimulation parameters in the format required by the stimulation controller in SoC. This format includes the most significant bit (MSB) and least significant bit (LSB) bit groups which define the stimulation pulse width and amplitude for each channel. As the packet for each stimulus data point is created it is immediately sent to the SoC in real-time. The SoC's stimulation controller configures internal registers with the bits from the data packet received and activates the stimulus current pulses in each channel accordingly. The process repeats at the predefined stimulation sample rate of the desired biomimetic stimulus waveform.

When the system is used to enable stimulation with randomized Inter-Pulse-Intervals (IPI), the user enters the average required stimulation IPI into the GUI device. The device generates an array of IPI following an exponential distribution with the required average following the equation:

$$T_n = \frac{ln(U)}{\lambda} \quad (1),$$

where T_n is the pulse period for the n-th pulse, U is uniform probability distribution in the range [0, 1], and λ is the desired mean of IPI. An array containing the parameters of the stimulation current pulses and the randomized IPI values are then sent to the control unit. The remaining control logic flow is the same as that of the biomimetic stimulation.

Figure 16 shows a photo of the biomimetic stimulator prototype with a size of 14 × 10 × 5.5 cm^3. The SoC is packaged in a QFP package to interface with peripheral electronics. 32 stimulation channels are available in the current package. Both the microcontroller board and DC-DC converter board are commercialized evaluation board. Other parts in the system including level shifter, low dropout regulators, and rechargeable battery are arranged underneath those three components.

Figure 16. The physical implementation of the portable biomimetic stimulation system.

Chapter 3
Bench-top Test Results

In this chapter, the bench-top test results of the implantable system and biomimetic stimulation system are both presented. The aging test for the implantable system is also demonstrated.

3.1 Bench-Top Test of the Implantable System

The implant system supports bi-directional operation for closed-loop neuromodulation, in which the command is transmitted from the external side to the implant side to configure the implant to generate stimulation, i.e. forward link operation, while the recorded physiological data is transmitted from the implant side to the external side for further signal processing, i.e. reverse link operation. This section presents the test results of both forward link and reverse link operations.

3.1.1 Forward Link Operation

The test setup for forward link operation is shown in Figure 17. The miniaturized bioelectronic implant was powered and configured by the rendezvous device (RD) through inductive links with a separation of 2 mm between the primary side and the secondary side coils. A graphical user interface (GUI) on an android tablet developed by our group wirelessly controlled the RD to generate the power and data signals required by the implant [29].

Bench-top test results validated the forward link operation of the implantable system. Representative waveforms generated by the RD are shown in Figure 18. The blue

trace (probe #1) shows the 2 MHz power signal on the primary side power coil. The cyan and pink traces (probe #2 and #3) are the 2 Mbps command sent from MCU and the 2 Mbps modulated signal on the primary side data coil, respectively. The modulated signal demonstrates DPSK characteristic, i.e. phase change occurs with a data of logic 1 while no phase change with a data of logic 0.

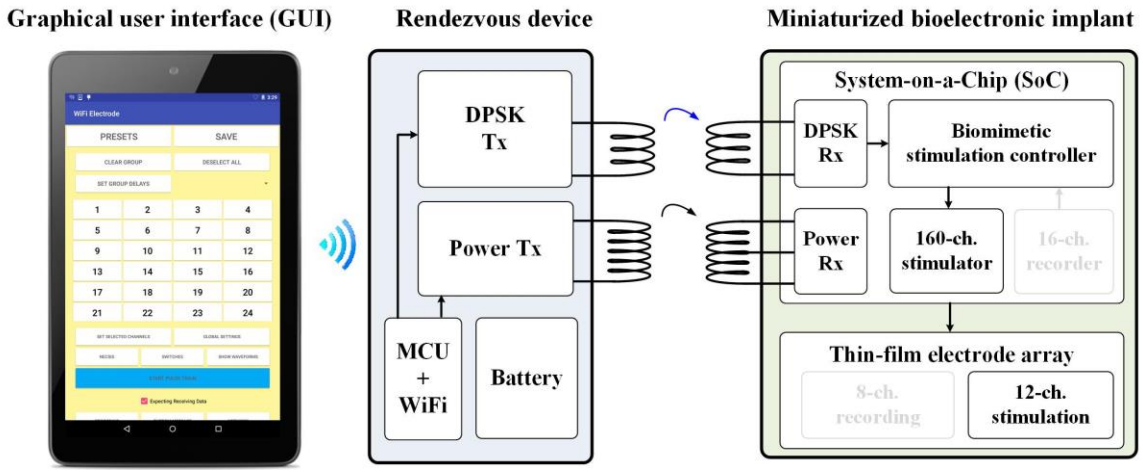

Figure 17. Bench-top test setup for forward link operation.

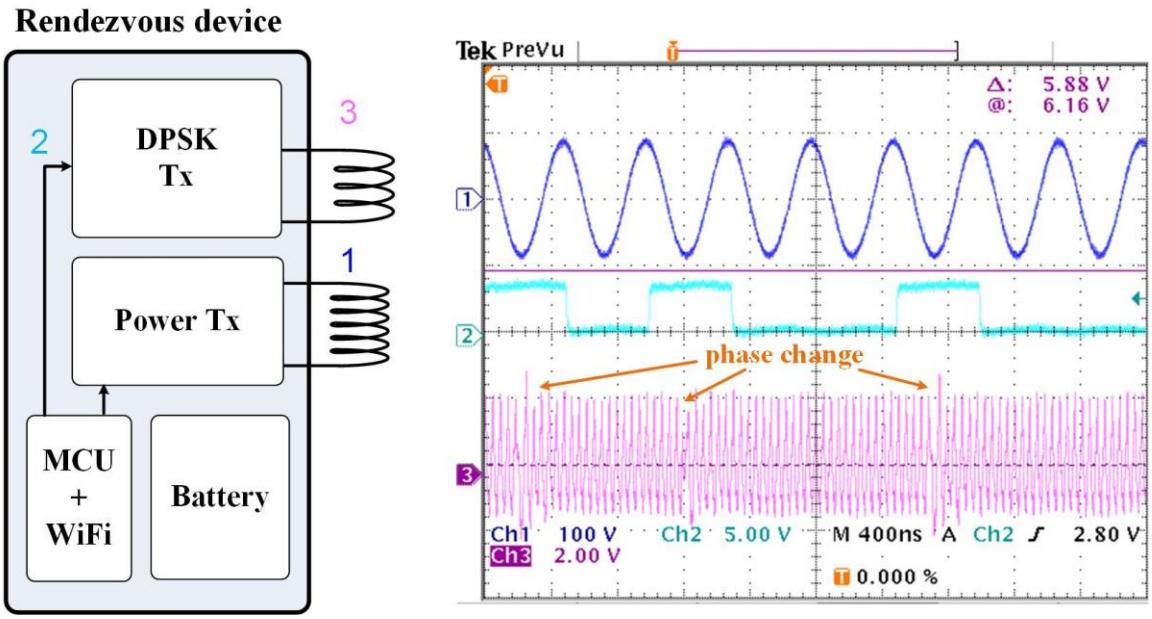

Figure 18. Waveforms generated by the rendezvous device on the bench-top.

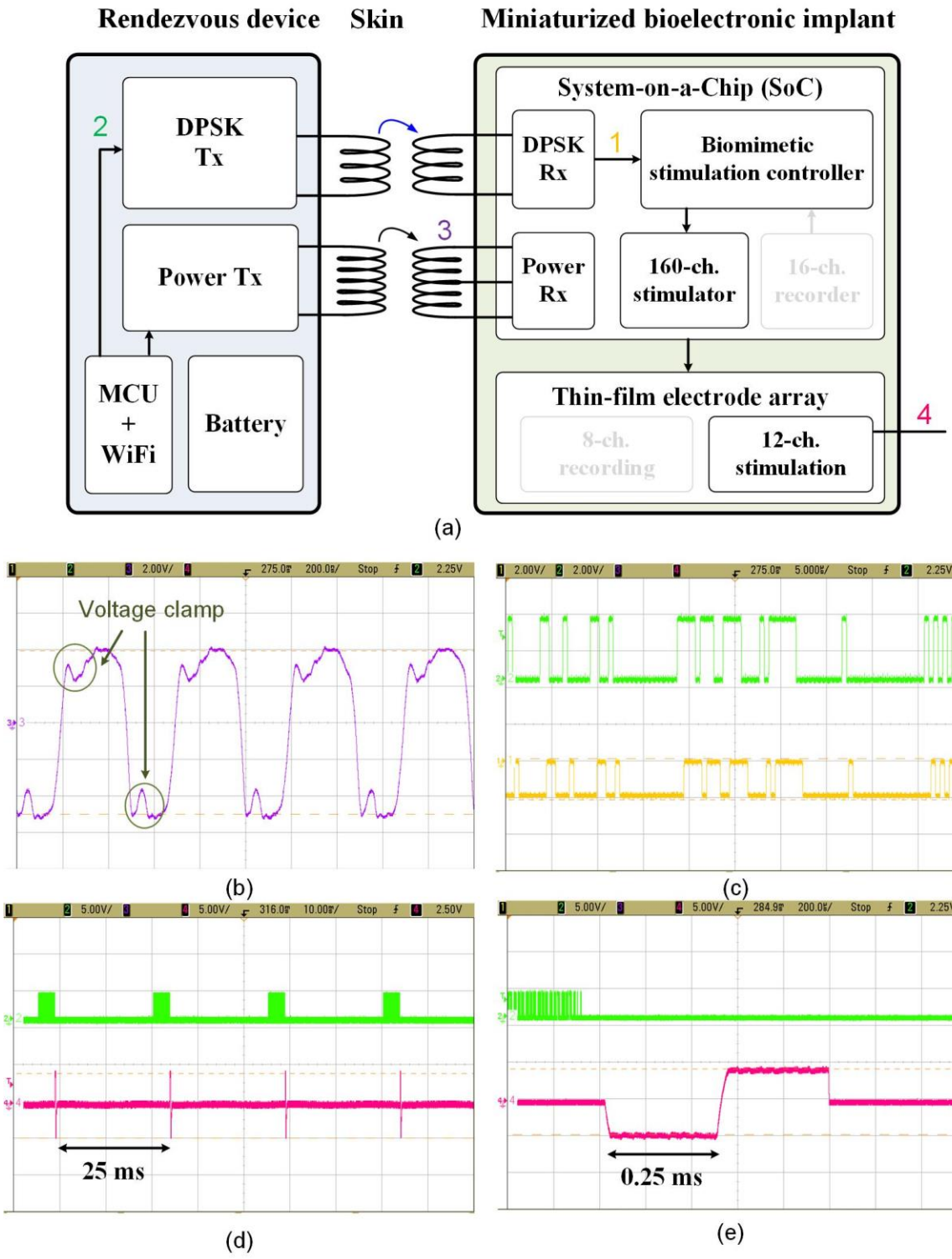

Figure 19. Waveforms of forward link operation on the bench-top. (a) System block diagram. (b) Power signal on the implant side. (c) The command transmitted by the rendezvous device (green trace) and command demodulated by the implant (yellow trace). (d) The command transmitted by the rendezvous device (green trace) and stimulation waveform (pink trace). (e) Zoom-in view of (d).

Figure 19 shows the representative waveforms of the implant system under forward link operation. The purple trace (probe #3) is the received low-voltage power signal on the implant side that supplies the on-chip ± 1.8 V. Note that the voltage clamp at the peak of the sinewave is due to the turn-on event of the rectifier in the wireless SoC, which is an indication of implant functioning [30]. The green and yellow traces (probe #2 and #1) are the commands sent by the RD and the command demodulated by the on-chip DPSK receiver in the implant, respectively. A 100% correct rate of command transmission, as shown in Figure 19(c), is necessary to generate the stimulation current. The pink trace (probe #4) is the stimulation waveform directly probed on the electrode array without load. A representative stimulation pattern with a frequency of 40 Hz and a pulse width of 25 ms is shown in Figure 19. The implant system also supports charge cancellation function for biphasic stimuli to eliminate the charge imbalance issue (Figure 20).

Figure 20. Demonstration of charge cancellation function. (a) Charge cancellation is OFF. (b) Charge cancellation is ON.

3.1.2 Reverse Link Operation

In this subsection, reverse link operation is demonstrated by the wireless recording of electromyography (EMG) signal that is a biomarker for closed-loop epidural stimulation [13]. The test setup for reverse link operation is shown in Figure 21. The powering and configuration of the miniaturized bioelectronic implant for reverse link operation was achieved by a successful forward link operation presented in Subsection 3.1.1. The EMG signal recorded by the implant was sent to the RD through the inductive data link, and the RD relayed the data to the graphical user interface (GUI) via WiFi for signal reconstruction. Note that the reverse link test was conducted incrementally. In this preliminary test, the EMG signal was pre-amplified and directly fed into analog-to-digital converter (ADC) input (signal point B in Figure 21) to bypass the noise-sensitive analog front-end. The front-end circuitry will be included in the test in the future. The performance of the reverse link was characterized by comparing the transmitted EMG (signal point B in Figure 21) with the reconstructed EMG (signal point G in Figure 21). Integrated EMG analysis (area under the curve of the rectified signal) was also performed.

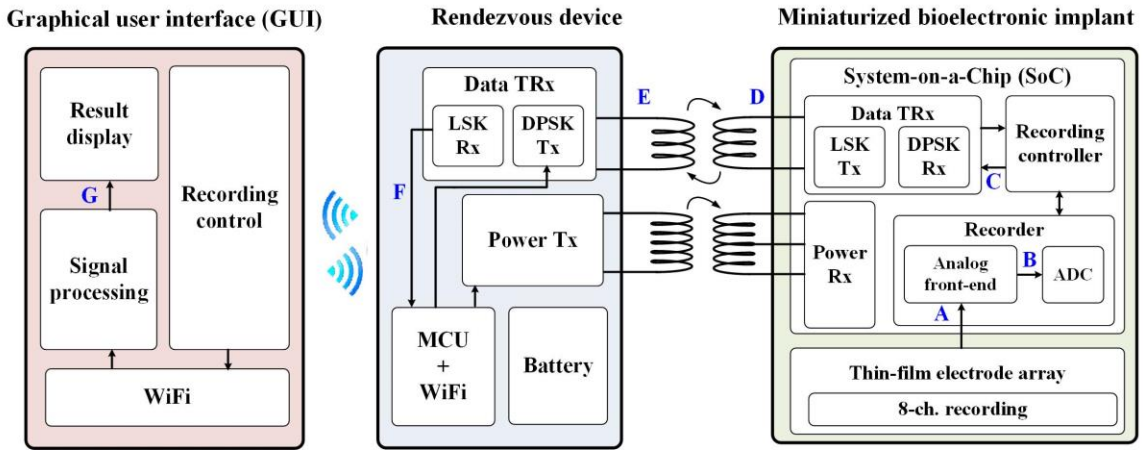

Figure 21. Bench-top test setup for reverse link operation.

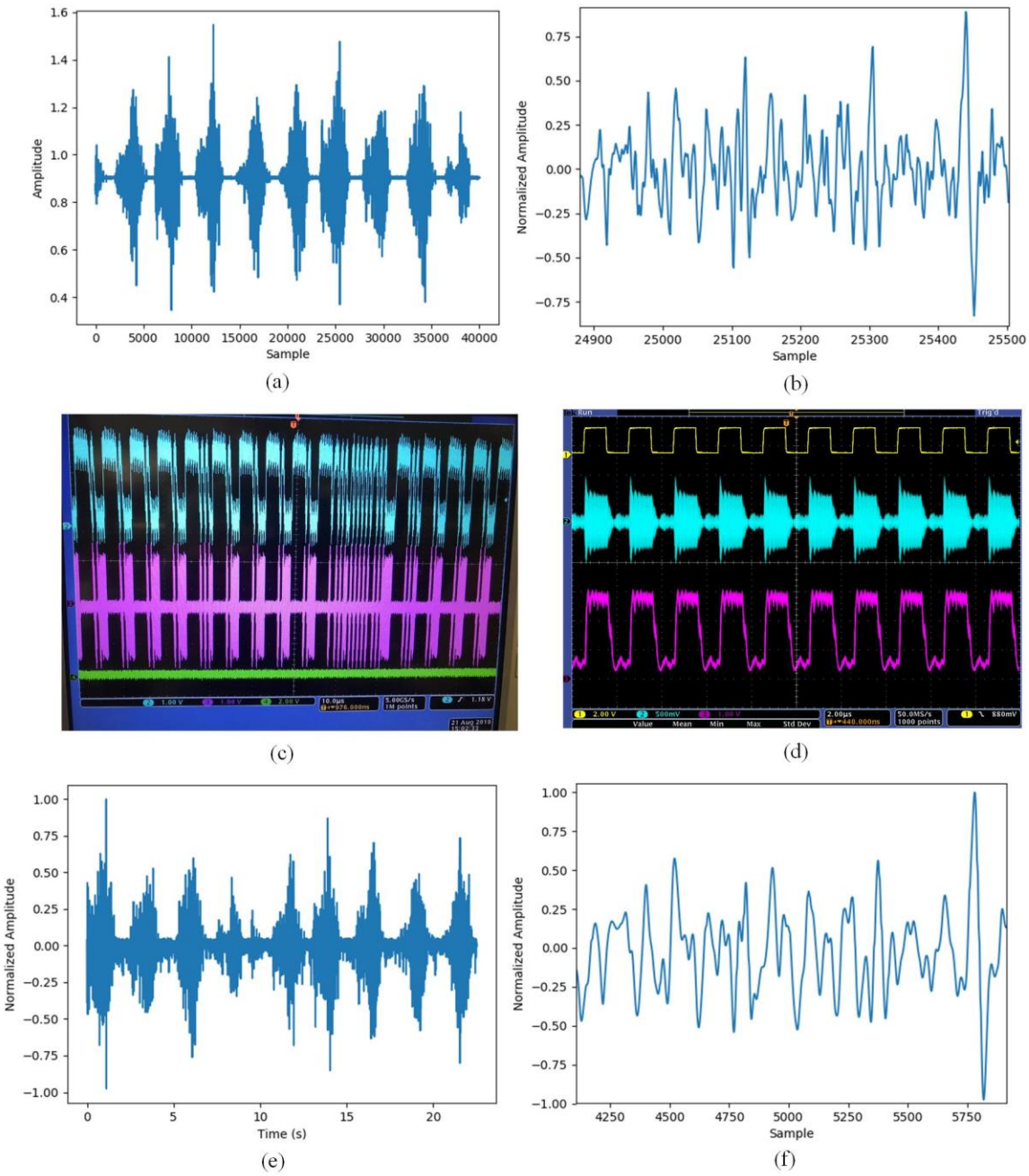

Figure 22. Measured results of the reverse link test. (a) Simulated EMG fed into the ADC input (signal point B in Figure 21); (b) zoom-in view of (a); (c) example waveform demonstrating the function of LSK transceiver. Blue trace is the output of LSK receiver (signal point F in Figure 21) while pink trace is waveform on the secondary side coil (signal point D in Figure 21); (d) another example waveform demonstrating the function of LSK transceiver. Yellow trace, blue trace, and pink trace are the input of LSK transmitter (signal point C in Figure 21), waveform on the primary side coil (signal point E in Figure 21), and output of LSK receiver (signal point F in Figure 21), respectively; (e) Reconstructed EMG signal on the GUI (signal point G in Figure 21); (f) zoom-in view of (e).

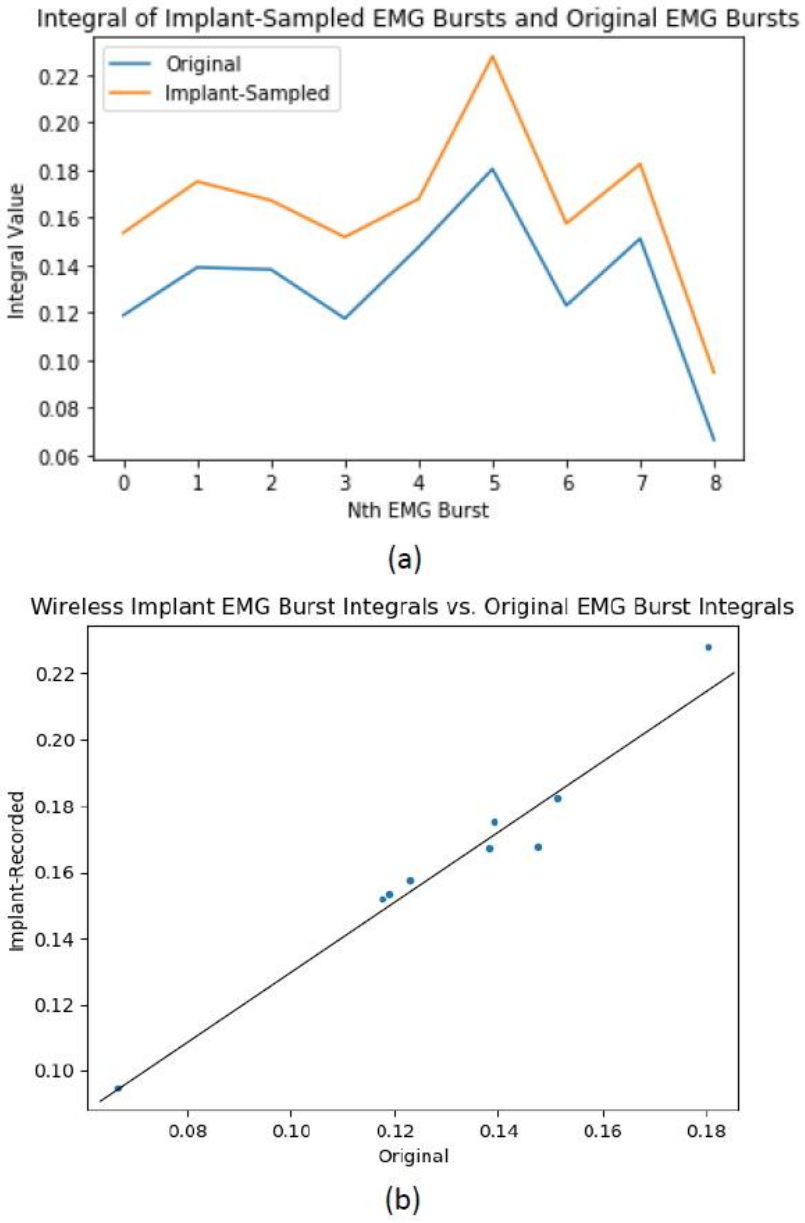

Figure 23. (a) Integrated power of the transmitted and reconstructed EMG bursts. (b) Regression plot of the integrated power of the transmitted and reconstructed EMG bursts.

Experimental results validated the reverse link operation of the implant system (Figure 22). All circuit blocks involved in this preliminary reverse link test functioned correctly. The received reconstructed EMG bears similarities to the transmitted simulated EMG as desired. The similarities include details of motor neurons potentials (as in Figure 22(b, f)), and the integrated power of the EMG bursts (Figure 23(a)). The integrated

EMG analysis indicated that each received reconstructed EMG burst is biased higher in power, relative to the corresponding transmitted burst (Figure 23 (a)). This added power constant is the white noise added by the system, as expected. Still, the relative powers between true EMG bursts and received EMG bursts are successfully preserved. A linear correlation between the integrated power of transmitted EMG bursts and reconstructed EMG bursts is shown (Figure 23 (b)).

3.2 AGING TEST OF THE IMPLANTABLE SYSTEM

Aging tests were conducted to investigate the lifespan of the bioelectronic implant for chronic implantation. Factors that shorten the lifespan of the implant include electrode degradation and deterioration of epoxy encapsulation. The degradation of electrode stems from electrochemical reactions happened in the electrode-electrolyte interface, which results in an increase in electrode impedance. The impedance increase degrades the quality of the electrode for both operations of stimulation and recording [31]. In a current mode stimulation, a high impedance leads to a high induced voltage on the electrode, which might induce an undesired electrochemical reaction that is harmful to cells. For the recording, a high impedance results in a high noise that makes the recording of weak neural spikes even difficult. The electrode degradation due to aging is thus an issue needed to be considered. On the other hand, deterioration of epoxy encapsulation that causes leakage of body fluid into the implant also shortens the device's lifespan [32]. Commercially available implantable devices utilize hermetically sealed housing to protect the electronics [26, 27]. Those housings are made of a material with a low water permeability rate which ensures device functionality over decades. However, as our bioelectronic implant is used for short-term implantation, hermetic housing is an

overdesign for our application. An economic but sufficient alternative, which is epoxy, is thus used to encapsulate the implant, and the reliability of this approach needs to be investigated.

The desired lifespan of the proposed bioelectronic implant was determined by applications presented in this dissertation: 1) intestinal stimulation to facilitate intestinal motility in a porcine model (Chapter 4), and 2) epidural stimulation to recover motor function after spinal cord injury in a rat model (Chapter 5). Based on the experimental protocol designed by our collaborative physiologists, the planned implantation duration for intestinal stimulation and for epidural stimulation are two days and four weeks, respectively. Considering the worst case, the desired aging of the implant was set to be four weeks with the implant delivering the stimulation protocol for epidural stimulation.

The lifetime of the bioelectronic implant was evaluated by two aging tests. Firstly, the electrode degradation was characterized by an *in-vitro* accelerated aging test using a custom-made electrode array that was fabricated by the same process and had the same electrode dimension with the electrode on the implant. A stimulation protocol with 150 μA amplitude and 0.2 ms pulse width at 40 Hz for epidural stimulation was delivered to the electrode during the aging test. Secondly, the reliability of the epoxy encapsulation approach was validated *in-vitro* using an epoxy encapsulated implant.

3.2.1 Electrode Array

The accelerated aging test showed that the equivalent survival time for 12 out of 12 electrodes on the custom-made electrode array was more than four weeks and 10 out of 12 electrodes are more than two years under the stimulation protocol of 150 μA, 0.2ms at 40Hz for 4 Hrs/day. This protocol specified by the collaborative physiologist provides

420,480,000 stimulus pulses in two years. The same amount of stimulus with the same current intensity and the pulse width was applied to the electrode array during the period of the accelerated aging test. The aging test was conducted for 37.1 days at 80°C, which is equivalent to aging survival of two years at 37°C according to the Arrhenius equation [33]:

$$AAF = Q_{10}^{[(T_{AA}-T_{RT})/10]} \quad (2),$$

where Q_{10} is the aging factor (typically set to 2), T_{RT} is the ambient temperature (37°C for the implant) and T_{AA} is the accelerated aging temperature.

Figure 24 shows the experimental setup. In Figure 24(a), a glass bottle filled with a 0.9% saline solution was placed in an isotemp oven (OV701F, Thermo Fisher Scientific, MA) at a constant temperature of 80°C. A custom-designed lid sealed on the bottle held the electrode array and ensured full immersion of the electrodes in the solution. Figure 25 shows the side view and top view of the sealed glass bottle along with the electrode array as well as the custom-designed lid. The electrode array was then wire-connected to a breadboard outside the oven through the oven access hole (Figure 24(b)). The breadboard served as an interface to connect the electrode array with the stimulus generator as well as the oscilloscope. The oscilloscope enabled the real-time monitoring of the electrode overpotential, thus eliminating the routine removal of the electrode for EIS characterization. As a result, a significant saving in testing time was achieved.

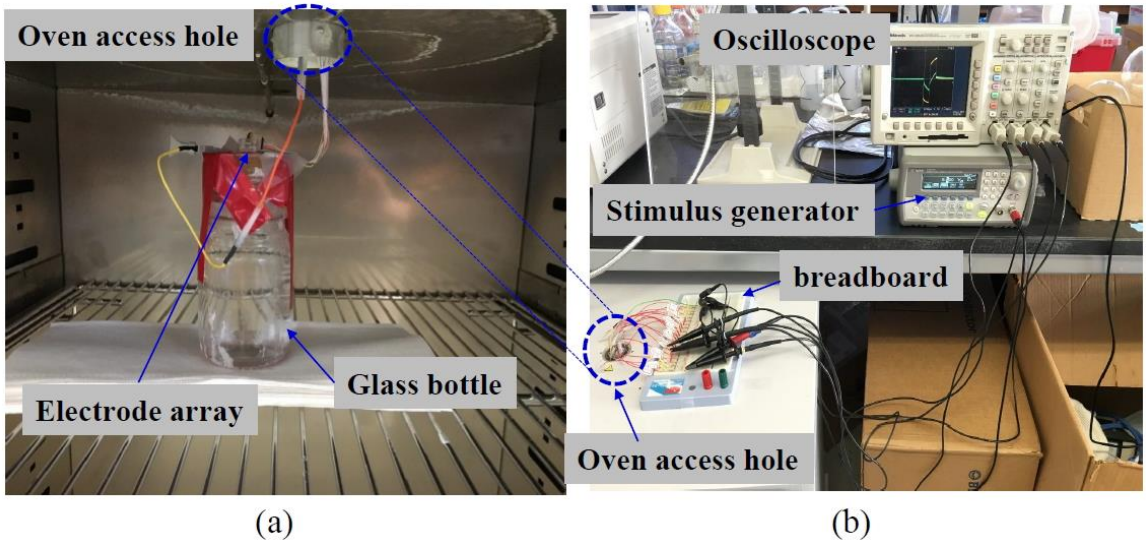

Figure 24. Setup of the accelerated aging test. (a) The oven inside provides a constant temperature environment. (b) Oven outside.

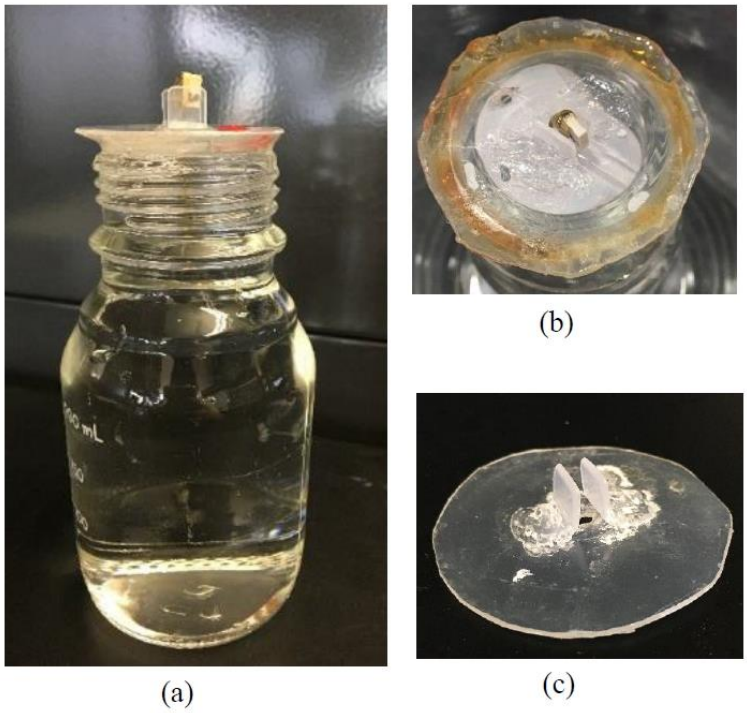

Figure 25. (a)-(b) Side view and top view photo of the sealed glass bottle along with the electrode array. (c) Photo of the custom-designed lid.

Figure 26 shows the measured electrochemical impedance spectroscopy (EIS) result of the electrode array over the testing period. 12 out of 12 electrodes have an impedance < 10 kΩ after four equivalent weeks, which meets the requirement. Moreover, 10 out of 12 electrodes have an impedance < 10 kΩ after two equivalent years of testing, suggesting that the electrode array also had the potential for long-term implantation.

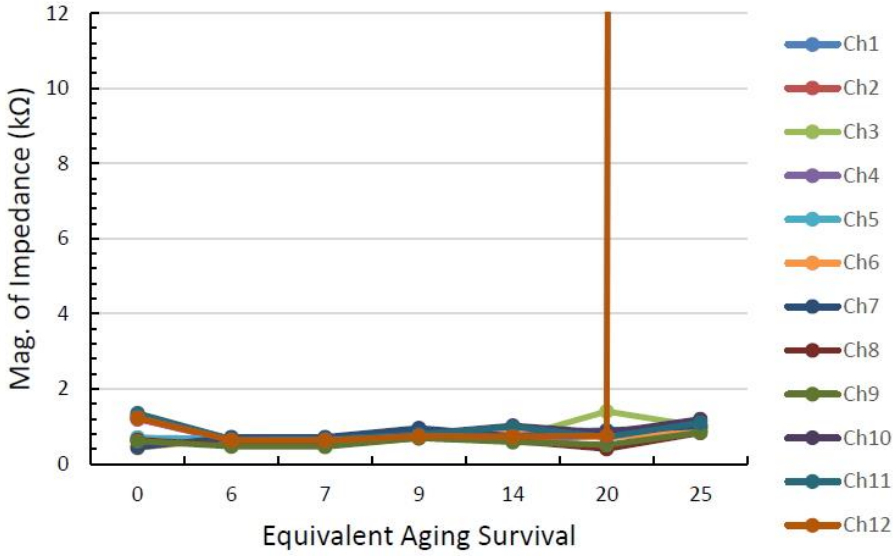

Figure 26. Measured EIS result of the electrode array in the accelerated aging test.

3.2.2 Bioelectronic Implant

The bioelectronic implant survived for 28 days in the saline at 37°C, which validates the epoxy encapsulation of implant for the *in-vivo* test. It is critical to note that because of the limited quantity of the fully functional implant, those valuable fully functional implants will be kept for the future animal experiments while the partially functional implants were used in this aging test to validate the epoxy encapsulation. During the aging test, the encapsulated implant was immersed in a 0.9% saline solution and its functionality was characterized daily. In order to eliminate the daily routine of setting up the functional test, a test platform that enables real-time monitoring of the

implant's functionality was developed. The experiment setup is illustrated in Figure 27. The implant was fully immersed in a glass beaker full of saline in an isotemp oven (OV701F, Thermo Fisher Scientific, MA) that provides a constant 37°C environment. The primary side power coil of the external unit was attached to the bottom of the beaker and aligned with the secondary side power coil of the implant. The primary side power coil was wire-connected to the rendezvous device (RD) outside the oven through the oven access hole. The RD delivered the required power for implant operation through the primary side coil. The wires that accessed the implant internal signals were connected to the probes of the oscilloscope through the oven access hole, enabling real-time monitoring of the implant's functionality.

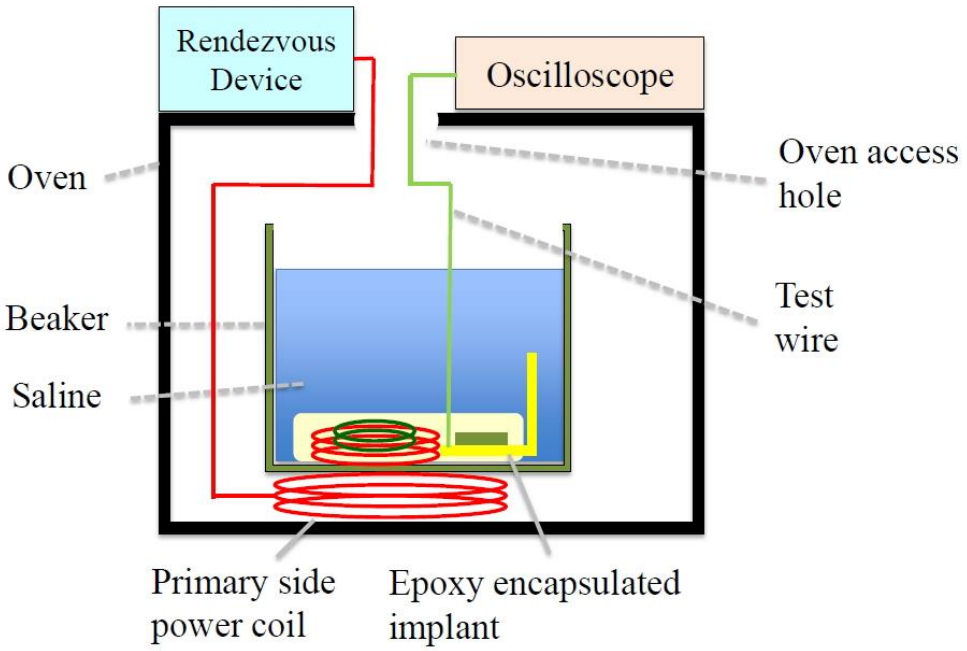

Figure 27. Setup of the aging test for the bioelectronic implant.

During the aging test, the 2 MHz power signal and the 16 MHz sampling clock for the DSPK receiver that were generated by a partially functional implant were

monitored as an indication of survival (Figure 28). The pink trace was the 2 MHz power signal received by the implant while the yellow trace showed the 16 MHz signal generated by the crystal oscillator supplied by the voltage rectifier in the wireless SoC. The two signals implied that the saline did not leak into the encapsulated implant and did not damage the SoC or the peripheral electronics, thus validating the feasibility of epoxy encapsulation for short-term implantation.

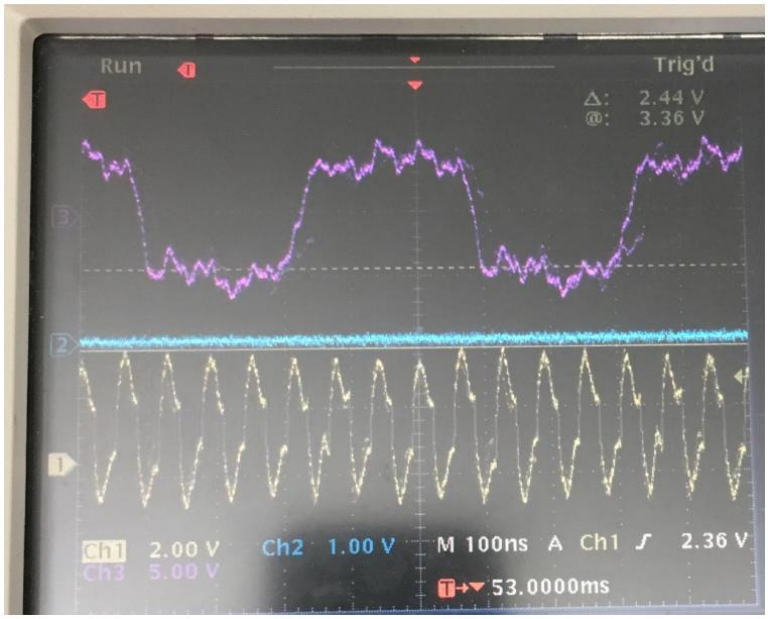

Figure 28. The measured waveform of the bioelectronic implant under the aging test.

3.3 BENCH-TOP TEST OF THE BIOMIMETIC STIMULATION SYSTEM

Bench-top tests were conducted to demonstrate the versatile waveforms generated by the biomimetic stimulation system, including randomized period pulse train for retinal stimulation applications and EMG-mimetic stimulation pattern for spinal cord stimulation. During testing, the stimulation system was wirelessly controlled by an App in an Android tablet through the WiFi link. Each stimulation output channel was connected to a 10 kΩ resistive load. Notably, the App was upgraded from our prior work

to support the configuration of each individual pulse required by biomimetic stimulation [29].

A demonstration of the randomized period pulse train is shown in Figure 29. The resulting multi-channel pulse trains exhibit random Inter-Pulse-Intervals (IPI), which follows an exponential random distribution and has been shown to reduce undesired neural adaptation in epiretinal stimulation [11]. The mean period is 30 ms with current amplitudes set to 0.5 mA and pulse width set between 1 and 4 ms among the available channels. This specific application only requires one random IPI pattern but does not impose a requirement for relative timing between multiple channels. Yet the presented logic design supports randomness in relative timing between channels if needed.

Figure 30 demonstrates the stimulator's ability to generate a biomimetic waveform. Figure 30(a) shows two signals with the desired stimulation waveform based on EMG recordings from the tibialis anterior (TA) of a rat during stepping. Figure 30(b) shows the corresponding EMG-mimetic output generated by the stimulator. The resolution of the output current amplitude supported by the SoC is 4 bits (digital-to-analog converter) + 3 bits (variable-gain current mirror). The temporal resolution of this example's waveform is 500 μs, measured from the start of one pulse to the next one. Within this period there is a 100 μs gap with a null output, which appears between each two consecutive current samples in Figure 30(b). This gap is required to transmit a command from the control unit to the SoC's stimulation controllers and process it by the controller. It is hypothesized that the presence and the exact length of this gap will not affect the response of neural tissue as it much shorter than the refractory period of an individual neural cell, i.e. 1-2 ms [34]. One future plan is to evaluate this hypothesis by

using the presented device in the future *in-vivo* study. Additionally, the gap can be removed by combining two stimulation channels as shown in Figure 31.

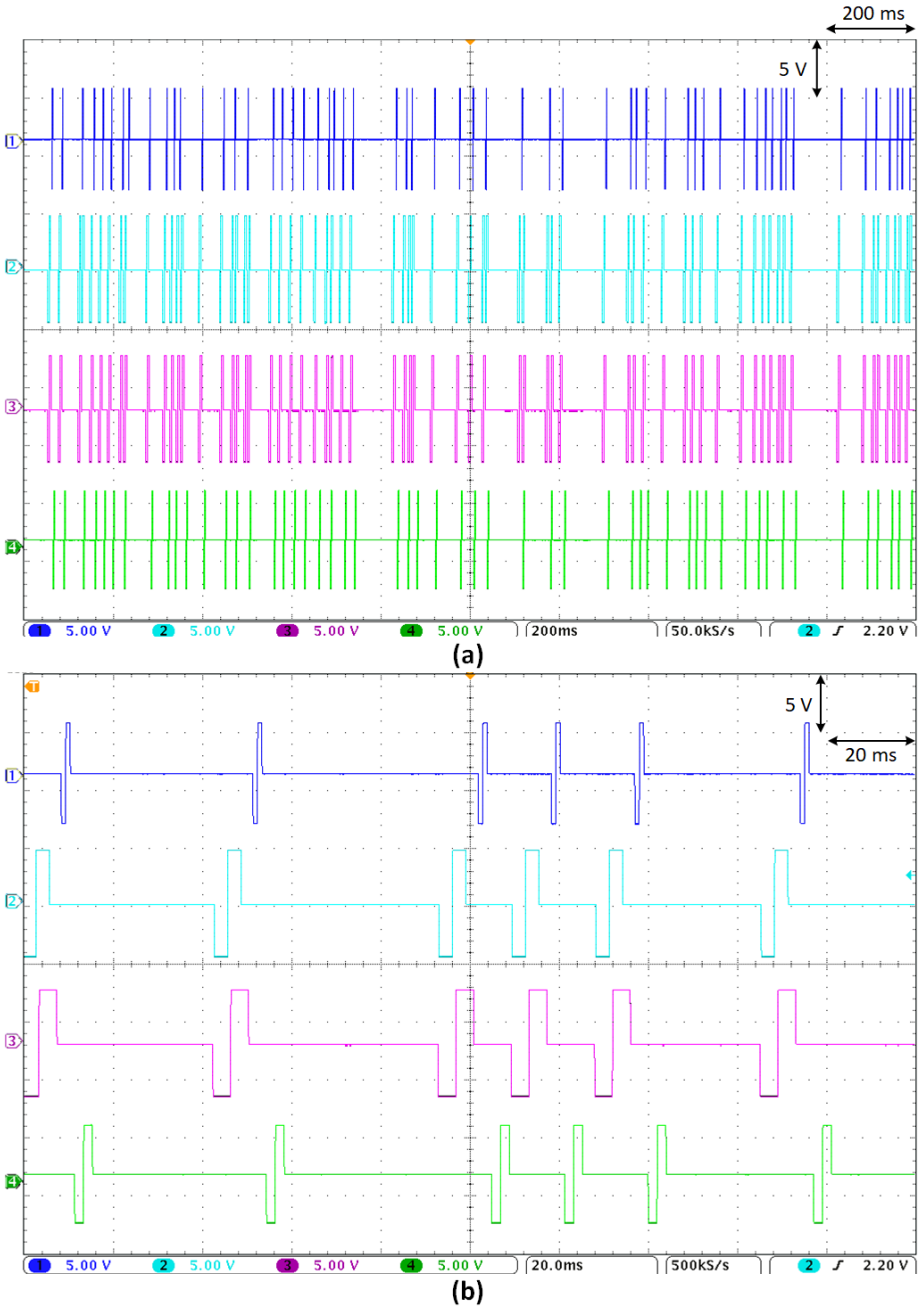

Figure 29. (a) Measured multi-channel simulation with random IPI following exponential random distribution. Each stimulation channel has a mean IPI of 30 ms and an output current of 500 µA. (b) Magnified view shows the different pulse widths and start delays among different channels.

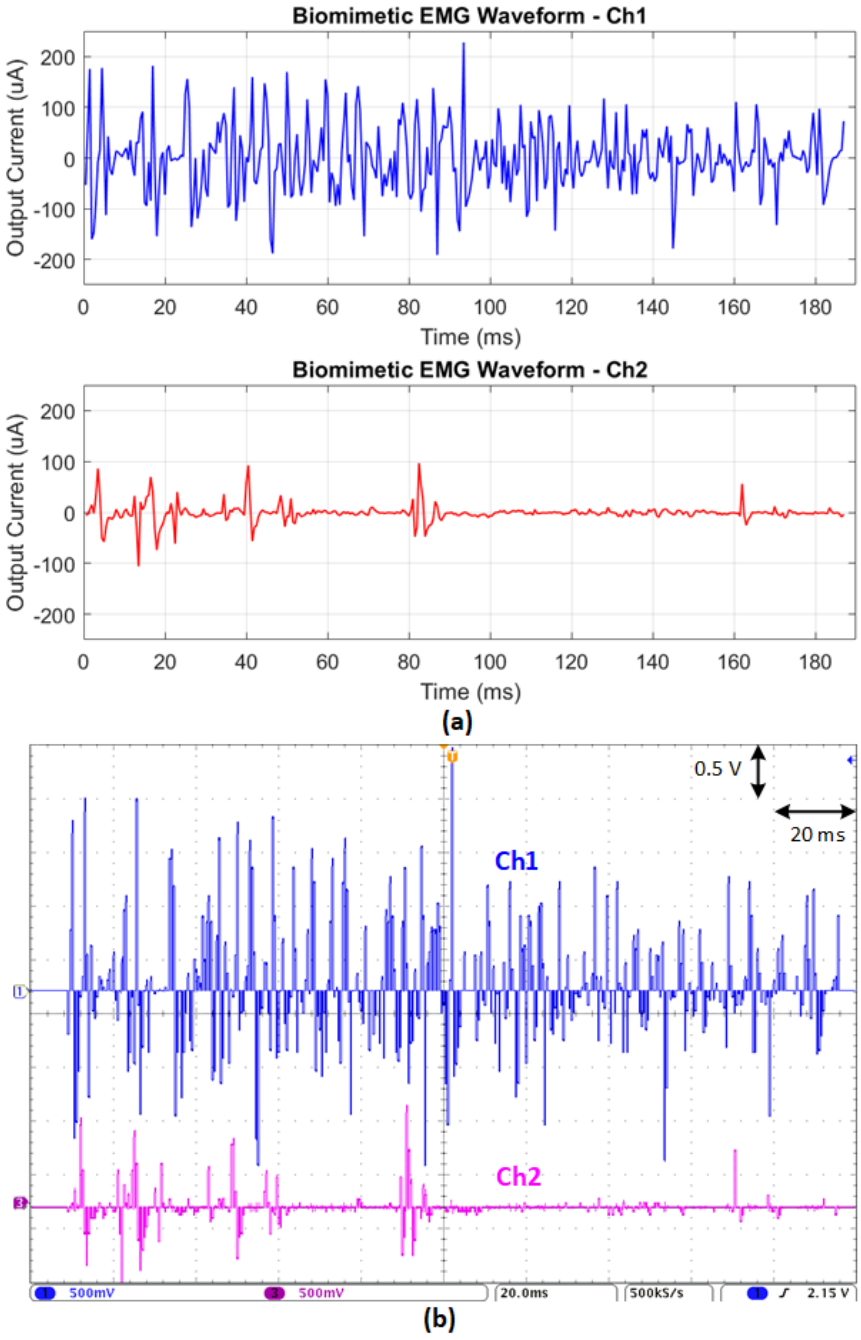

Figure 30. Bench-top demonstration of multi-channel biomimetic waveform stimulation mimicking a recorded EMG waveform, which has been shown to be effective in epidural spinal cord stimulation for restoring motor function [9, 14]. (a) Desired biomimetic stimulation waveform. (b) The output of the prototype stimulator captured with an oscilloscope.

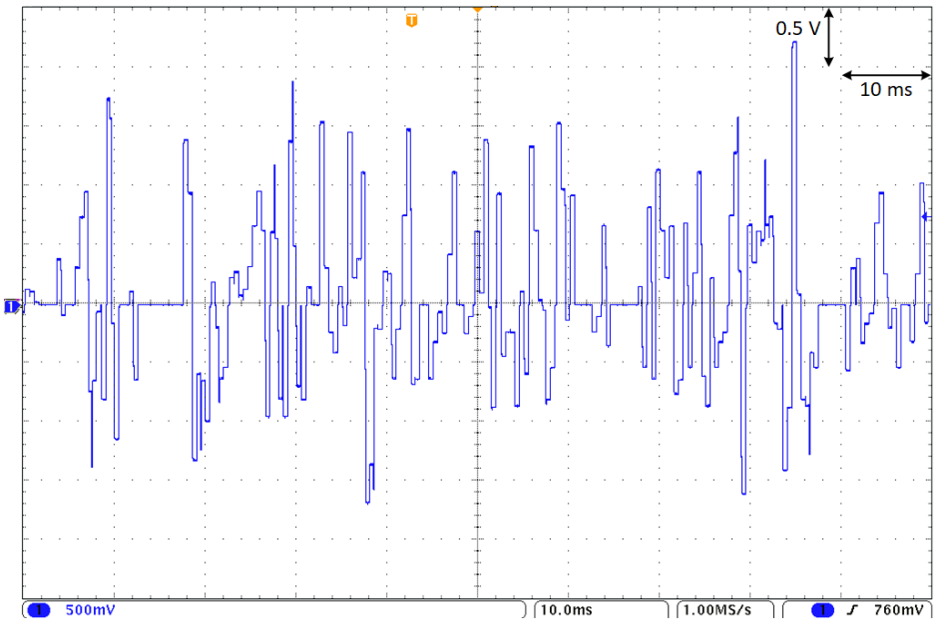

Figure 31. A continuous biomimetic current waveform is achieved by combining multiple channels together into a single output.

One potential issue of the biomimetic stimulation, e.g. EMG-mimetic pattern, is the charge imbalance induced by a non-symmetric waveform that might cause neural damage. This can be addressed by the charge cancellation switch in the SoC, which passively dissipates the accumulated charge in the electrode/tissue interface. The timing of the discharge behavior can be controlled through a predetermined setting, which allows the researchers the flexibility to enable this function and tailor it for various stimulation protocols.

Chapter 4
Pre-Clinical Trial: Intestinal Stimulation for Facilitating Gastrointestinal Motility

4.1 BACKGROUND

The estimated annual healthcare expenditures for gastrointestinal (GI) motility disorders is USD 29 billion, which imposes a significant burden on the U.S. healthcare system [35]. GI motility disorder is defined as the abnormal movement behavior of the GI tract that affects the function of mixing and propelling food. This can happen to any segment of the GI tract, including the esophagus (e.g., dysphagia, achalasia), stomach (e.g., gastroparesis, gastroesophageal reflux disease), and intestines (e.g., diarrhea, constipation). The pathophysiological mechanism of GI motility disorders is not completely understood due to the complex, cooperative mechanisms between the smooth muscle cells (SMC), interstitial cells of Cajal (ICC), enteric nervous system, central nervous system, and hormones [36, 37]. This gap of knowledge impedes the development of efficacious therapies for improving GI motility. Although a number of pharmaceutical drugs have been developed, most of them do not completely alleviate GI dysmotility [38]. Moreover, the use of drugs faces the challenge of target specificity, as it is difficult to precisely control the dose of pharmacological agents.

A potential treatment alternative for GI motility disorders is GI electrical stimulation. The fundamental principle behind this therapy is to electrically modulate myoelectric activity that controls smooth muscle contraction/relaxation, i.e., slow waves and spikes [39]. A slow wave is a rhythmical electrical event originating from ICC, while

a spike is the action potential that stems from the inflow of calcium ions to the SMC. ICC and SMC are both regulated by the enteric nervous system in the GI tract [40, 41]. It is thus feasible to directly induce smooth muscle contraction through modulating SMC or indirectly via activating the ICC/myenteric network using GI electrical stimulation. Several studies have demonstrated the therapeutic potential of GI electrical stimulation in GI dysmotility, including gastric electrical stimulation for pharmaceutically intractable gastroparesis [42, 43], intestinal electrical stimulation for accelerating intestinal transit [44, 45], and colonic electrical stimulation for constipation [46, 47]. The potential mechanisms are either the stimulation of the SMC [42, 43] or the activation of the cholinergic or nitrergic pathways in the enteric nervous system [44-47].

Despite promising research results, the clinical applicability and usability of GI electrical stimulation for GI motility disorders are still limited due to the lack of appropriate implantable stimulation devices. In light of the fact that existing commercial implantable pulse generators (e.g., deep brain stimulator, spinal cord implant, vagus nerve stimulator [48-50]) have limited parameter programmability, the implantable GI stimulator should support a wide range of stimulation parameters (i.e., pulse width, current intensity, frequency), especially long-pulse stimuli to activate smooth muscle when necessary. Interestingly, even on the same GI segment, diverse stimulation parameters have been reported for improving GI dysmotility, e.g., colonic transit could be accelerated in rats by stimulation protocols of 4 ms, 10 mA, 40 Hz [51], and 0.3 ms, 5 mA, 10 Hz [52]. It is thus essential to develop a device capable of versatile stimulation parameters in order to customize an optimal stimulation strategy for each individual. This above feature is also critical, as the investigation of an optimal stimulation protocol for

effectively activating GI contraction and the sophisticated working mechanism of the GI tract is still ongoing. Another desired feature for GI implants is the miniaturized form factor. This would be clinically beneficial, as surgical invasiveness can be minimized during implantation. Existing commercial GI implants are bulky and only support stimuli with a very limited range of parameters, e.g., pulse width shorter than 1 ms [21, 53]. The short pulse width limits their usage in treating nausea and vomiting [53] or increasing the pressure of lower esophageal sphincter for relieving gastroesophageal reflux disease [21]. Both commercial devices might not be applicable to directly altering GI motility as most protocols for inducing GI contraction require a stimulation pulse greater than 1 ms [42-47]. In order to fill the technology gap, a miniaturized implantable GI stimulator supporting a wide range of stimulation parameters is needed.

We tailored the developed implantable system presented in Chapter 2 to fulfill the aforementioned needs (Figure 32). The wireless implant is encapsulated by biocompatible epoxy and implanted in the abdominal wall through midline abdominal incision. The rendezvous device (RD) carried by the subject receives user-defined commands from the graphical user interface (GUI) via the WiFi link and delivers power and command to configure the wireless implant through inductive links. A preliminary *in-vivo* chronic study was conducted using porcine models to investigate the potential of the system for accelerating intestinal transit. In order to ensure effective and safe intestinal stimulation, the experiment protocol was designed as follows: 1) the charge injection limit and impedance of the electrode-tissue interface were first characterized using cyclic voltammetry (CV) and two different impedance-measurement methods. This provides a guideline for a safe stimulation protocol that avoids any electrochemical

tissue-damaging reaction in the electrode-tissue interface [54]. 2) An acute *in-vivo* test using the electrode array was then performed to investigate the stimulation protocol that is also electrochemically safe for facilitating intestinal motility. 3) The wireless implant system was tested on the bench-top to ensure its capability of generating the desired stimulation pattern identified in the acute test. 4) A preliminary *in-vivo* chronic test was finally conducted to demonstrate the wireless implantable system as an effective tool for accelerating intestinal transit in porcine models. The use of all animals was approved by the UCLA Animal Research Committee (Institutional Review Board no. 2014-142-03E).

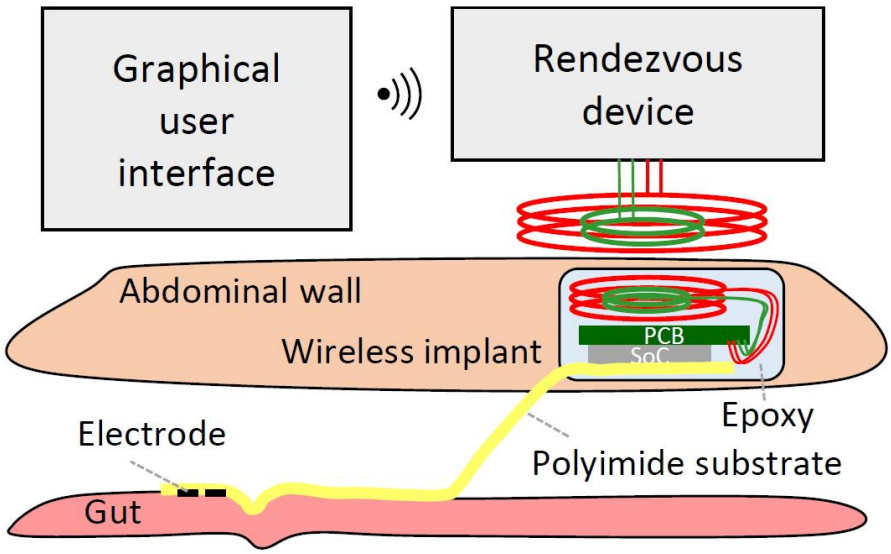

Figure 32. Illustration of using the developed wireless implant system for intestinal stimulation.

4.2 ELECTRODE CHARACTERIZATION

The electrode-saline interface and electrode-intestinal fluid interface were both characterized for stimulation-safety evaluation, as both extraluminal and intraluminal intestinal stimulation have been reported as potential treatments for intestinal dysmotility [44, 55]. A 0.1 M NaCl solution was used to mimic the extraluminal environment, while intraluminal intestinal fluid was extracted from a juvenile mini Yucatan pig. A

customized electrode array that was fabricated by the same process and had the same electrode dimension with the electrode array on the wireless implant was soaked separately in both saline and intestinal fluid. The charge injection limit, bioimpedance, and Randles cell model of both electrode-electrolyte interfaces were characterized using CV, electrochemical impedance spectroscopy (EIS), and the time-domain Randles cell model characterization method [56], respectively.

The measured cyclic voltammogram is shown in Figure 33, and all measured electrochemical properties are summarized in Table I. The electrochemical window of the electrode was [–0.9, 1 V] in both saline and intestinal fluid environments. Charge storage capacity (CSC) of the electrode, which defines the charge injection limit per stimulation phase, of the intestinal fluid group was 1.16 times higher than the saline group (10.68 vs. 9.19 μC). The EIS-measured impedance of the electrode at 1 kHz of the intestinal fluid group was 2.45 times higher than the saline (6.39 vs. 2.61 kΩ), which implies that the maximum allowable stimulation current without exceeding the compliance voltage of the stimulator was ~2.45 times smaller in the intestinal fluid than in saline. The measured Randles cell model of the electrode also provided the same insight, as R_S was 2.26 times larger in the intestinal-fluid group (3.69 vs. 1.63 kΩ). The product of R_{CT} and C_{dl}, i.e., the RC time constant, was comparable between the two groups (29.70 vs. 29.11 μs), suggesting that the required time to discharge residual electrical charge at the stimulation electrode was the same. According to this experiment result, extraluminal stimulation is more beneficial compared to intraluminal, as it allows a 2.45-fold higher stimulation current, with an acceptable penalty of 1.16-fold decrease in charge injection limit.

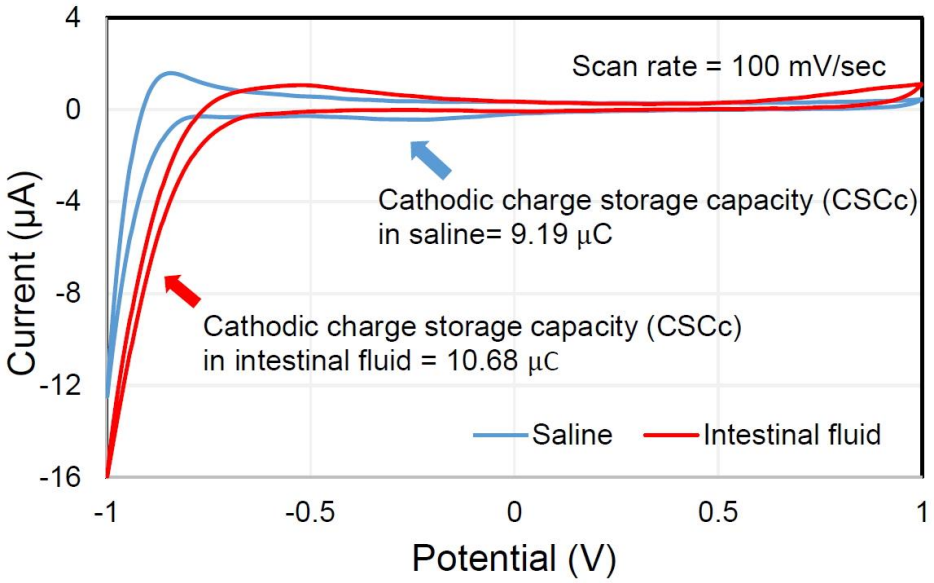

Figure 33. Measured cyclic voltammogram of the electrode array in saline and intestinal fluid.

Table I. Summary of measured electrochemical properties of electrode–intestinal fluid and electrode–saline interface.

Electrochemical Property	Saline	Intestinal Fluid
Cyclic voltammogram		
Electrochemical window (V)	[–0.9, 1]	[–0.9, 1]
Charge storage capacity (μC)	9.19	10.68
Electrochemical Impedance Spectroscopy (EIS)		
Magnitude@ 1 kHz (kΩ)	2.61	6.39
Phase@ 1 kHz (°)	–52.1	–53.9
Randles cell model characterization		
R_S (kΩ)	1.63	3.69
R_{CT} (kΩ)	2.12	4.7
C_{dl} (nF)	13.73	6.32

4.3 Stimulation-Parameter Identification in *In-Vivo* Acute Experiments

In-vivo acute tests using juvenile mini Yucatan pigs were conducted to investigate the effective and safe intestinal-stimulation protocol for improving intestinal dysmotility. Animal preparation and surgical procedures were described in our work [45]. During the

experiment, a midline laparotomy was performed, and a short segment of jejunum was identified and externalized. The jejunum was transected, and 5 mL of ultrasound gel was placed inside. The segment of jejunum was then monitored for 20 minutes, first under no stimulation, and then under electrical stimulation generated by our SoC via the customized electrode array laid on top of the exposed segment. The gel forced back out of the intestine via peristalsis was collected and weighed for each 20-minute time interval.

Effective stimulation parameters for increasing the rate of peristalsis were investigated in our previous work [45]. One set of biphasic current stimuli (100 Hz, 2 mA, and 2 ms) was obtained and was able to induce both local contraction and peristalsis. The result showed that in a 20-minute time period, an average of 0.51 grams of the gel was expelled without intestinal stimulation, while 1.67 grams of gel were expelled with stimulation ($n = 6$, $p < 0.05$) (Figure 34).

The potential mechanism is the activation of ICC or the local enteric nervous system by stimulation. The identified stimulation protocol is electrochemically safe in terms of charge injection limit. The stimulus with 2 mA intensity and 2 ms pulse width lead to a 4 μC charge per stimulation phase, which was smaller than the charge-storage capacity of the electrode (9.19 μC) characterized in the CV test. In addition, based on the Randles cell model of the electrode-tissue interface characterized in the impedance measurement, it could be estimated that the peak-to-peak voltage induced by this current stimulation pattern was around +/–7.5 V, which was within the compliance voltage of the stimulator.

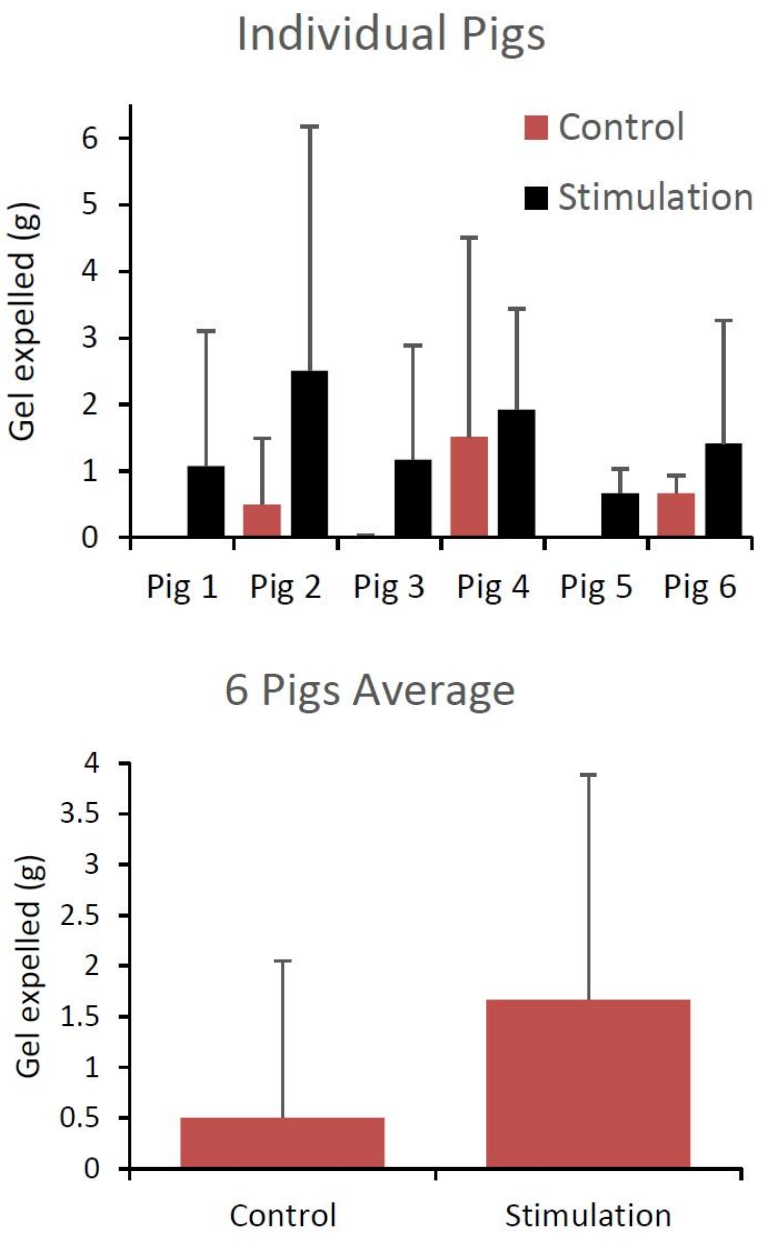

Figure 34. The measured weight of the expelled gel. (a) Results of individual pigs. (b) Averaged results.

4.4 System Bench-Top Test

The wireless implant system was tested on the bench-top to verify its capability of generating the desired stimulation protocol. The implant was powered and configured by the RD through inductive links with a separation of 2 cm between the primary side and

the secondary side coils. A GUI on an android tablet wirelessly controlled the RD to generate the power and data signals required by the implant [29]. The output of the stimulator was connected to a 1 kΩ resistor through PCB pads for current intensity characterization. A representative waveform to demonstrate the operation of the wireless implant system is shown in Figure 35.

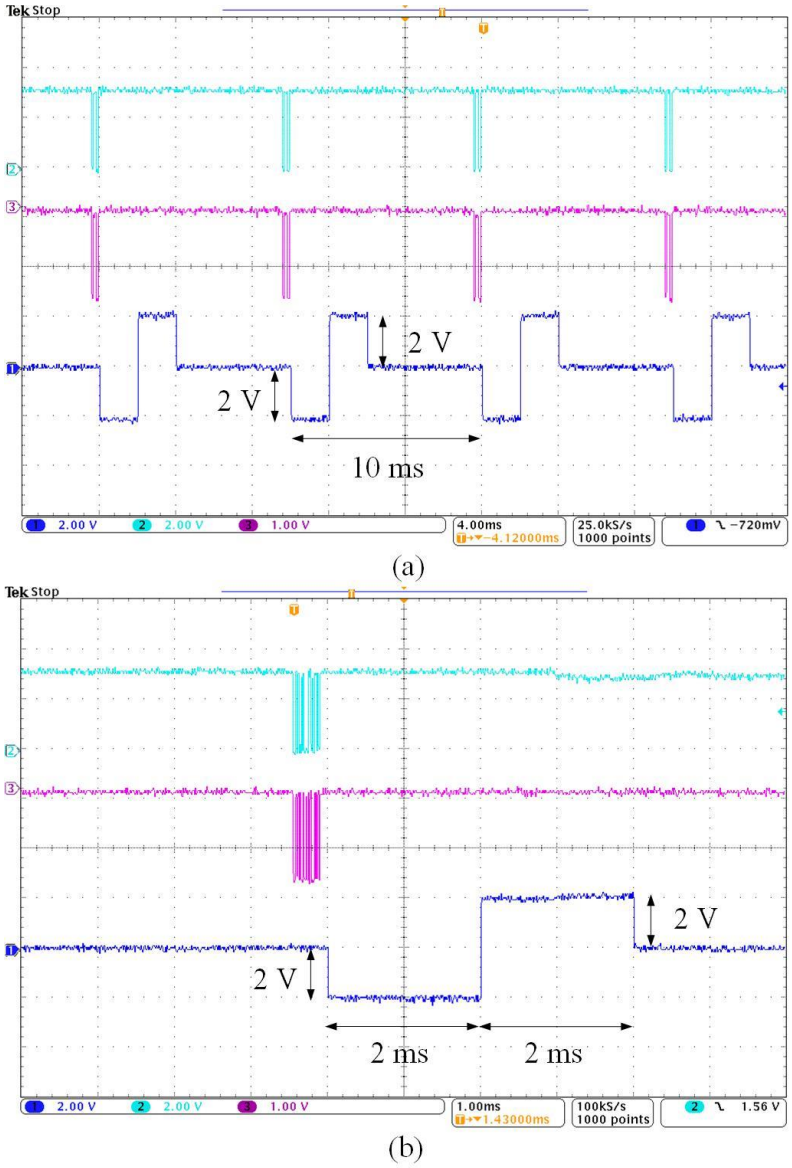

Figure 35. The 100 Hz, 2 mA, and 2 ms stimulus was generated by the wireless implant system on the bench-top. The cyan, pink, and blue traces are the command sent from the MCU in the RD, command demodulated by the DPSK receiver in the implant, and the induced output voltage waveform, respectively. The traces are presented in a time period of (a) 40 ms and (b) 10 ms.

4.5 PRELIMINARY *IN-VIVO* CHRONIC EXPERIMENTS

A preliminary *in-vivo* chronic study was performed to validate the wireless implant system and the identified stimulation protocol for accelerating intestinal motility. Four juvenile mini Yucatan pigs underwent a laparotomy to receive implants that were sterilized by ethylene oxide. Two of the four pigs were the control group that received the implants without turning on the stimulation, while the other two received active implants delivering the stimulation. The implant was placed inside a pouch created in the abdominal wall, and the electrode array was sutured on top of the intestine that was the proximal end of the jejunum identified by the ligament of Treitz. Fifteen metal beads were placed inside the intestine, about 5 cm above the segment where the electrode array was sutured. Right after surgery, an X-ray contrast was injected into the pig's stomach through a gastric tube and X-ray images were acquired. The implant was then wirelessly powered and configured through the RD to deliver the stimulation to the electrode that was in the middle column and closest to the tip of the array. Each pig was trained to wear a jacket that carried the RD before the surgery. The pigs were examined three times using X-ray: immediate after surgery, one day postoperative, and two days to monitor the transit of the X-ray contrast.

X-ray results showed that electrical stimulation likely facilitated intestinal transit as the contrast appeared in the rectum in Pig 4 on Day 1, earlier than in the other control pigs (Figure 36). The defecation of feces mixed with the X-ray contrast was also observed in Pig 4 on Day 1, but not clearly in other pigs. However, the movement of metal beads did not show coherent results in X-ray photography. The potential root cause is the small size and slippery surface of the metal beads that make the propelling of the

beads inside the GI tract challenging. Although our preliminary data show encouraging results, further studies involving more subjects should be conducted.

Intestinal-tissue histology was also performed to examine for any tissue damage due to stimulation (Figure 37). Three sections of jejunum were compared: normal jejunum distal to the surgical site (section 1), jejunum that was attached to the planar electrode array but did not receive stimulation (section 2), and jejunum that was attached to the planar electrode array and received stimulation (section 3). Sections 2 and 3 showed some mild inflammation and hemorrhage in the serosa and longitudinal muscle layer, likely related to the surgical manipulation of these sections of the intestine instead of the stimulation. These changes did not appear to be clinically significant. The three different sections appear otherwise comparable. There is no difference in the villi or crypts seen on these sections, and the submucosa and muscle layers also appear similar.

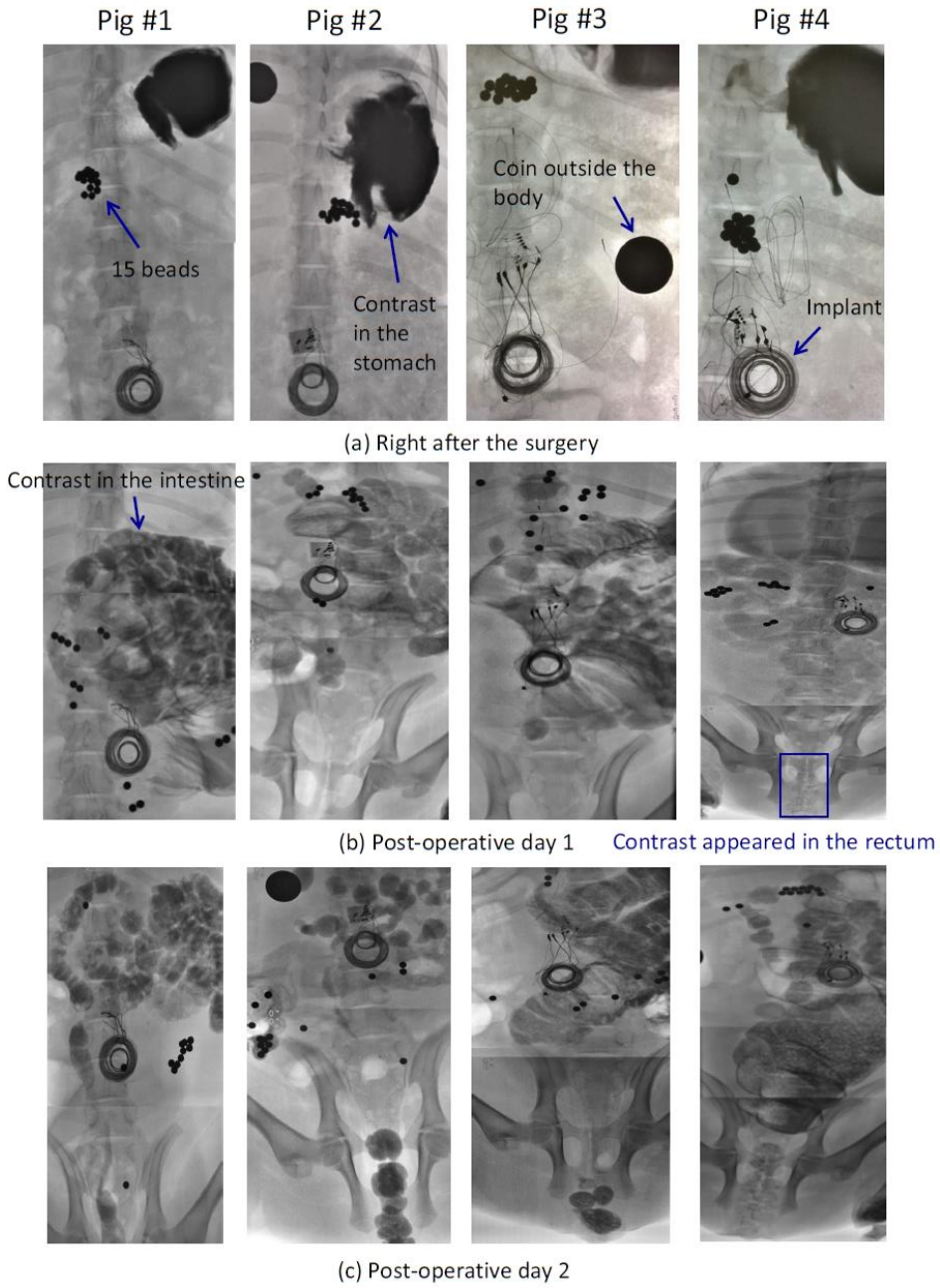

Figure 36. Intestinal transit examined through X-ray photography. Pigs 1 and 2 are the control group, while 3 and 4 are the experimental group. (a) Fifteen metal beads were inside the intestine, and X-ray contrast was in the pigs' stomach right after the surgery. (b) On postoperative Day 1, the contrast appeared in the rectum in Pig 4 with electrical stimulation, while the contrast had only moved to the intestines in other pigs, suggesting that electrical stimulation likely facilitates intestinal transit. The defecation of feces was also observable in Pig 4 but not in other pigs. (c) Contrast moved to the rectum in all pigs on postoperative Day 2.

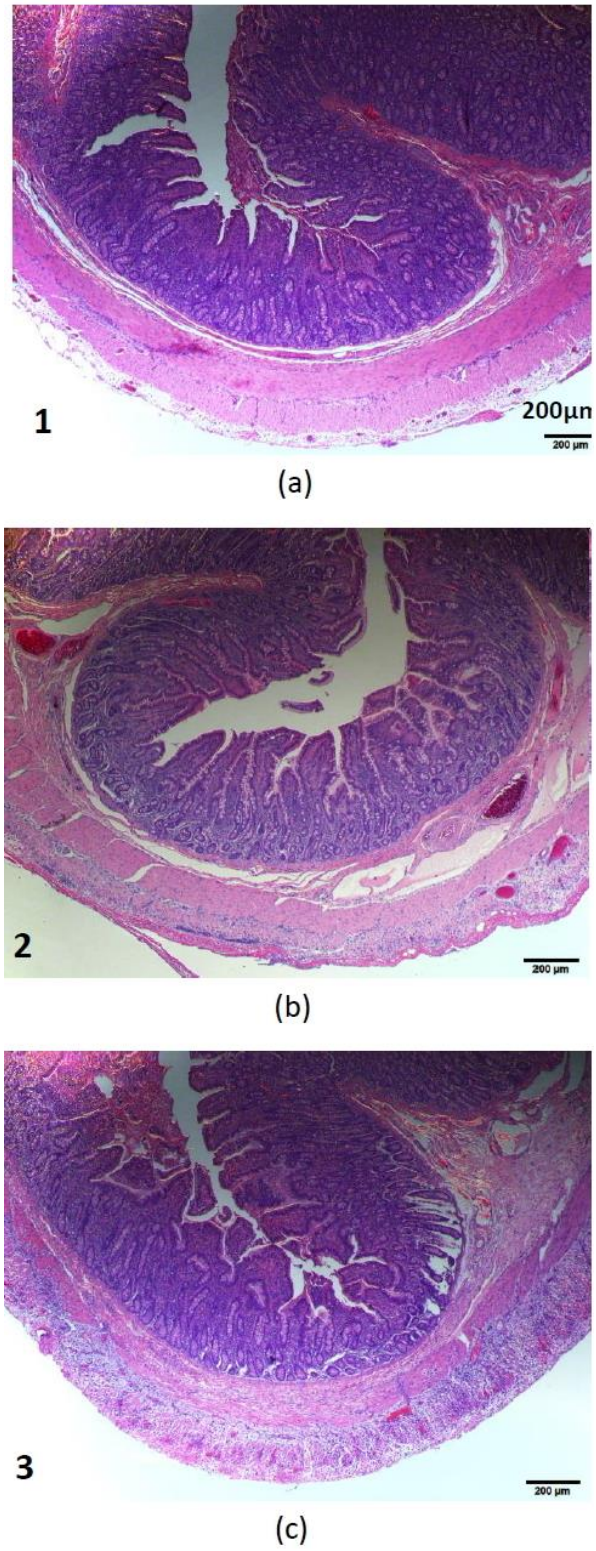

Figure 37. Intestinal-tissue histology. (a) Normal jejunum distal to the surgical site (section 1), (b) jejunum that was attached to planar electrode array but did not receive stimulation (section 2), and (c) jejunum that was attached to planar electrode array and received stimulation (section 3).

Chapter 5
Pre-Clinical Trial: Epidural Stimulation for Motor Function Recovery for the Spinal Cord Injured

5.1 BACKGROUND

The estimated number of spinal cord injury (SCI) patients in the U.S. in 2018 is 288,000 with an annual incidence of approximately 17,700 cases and the estimated lifetime cost per patient is > USD 1.1 million [57]. SCI is defined as the damage to the spinal cord that results in a temporary or permanent neurological deficit. Patients with SCI may lose their sensation, muscle function, or autonomic function in the parts of the body that are controlled by the spinal cord below the level of injury. This functional loss is due to the disruption of electrical impulse conduction in descending motor fibers from the motor cortex to the spinal motor neurons, and in the ascending somatosensory fibers from the spinal cord to the brain. Nevertheless, although SCI interrupts this cerebrospinal pathway, key planning, coordination, and effector centers above and below the injured spinal segment remain intact [8]. This provides the opportunity to recover the motor function after SCI by activating the intact spinal circuitries through epidural electrical stimulation [58-62]. It has been shown that epidural stimulation with periodic electrical pulses not only enables the brain to exploit the spared descending pathway in order to generate voluntary movement of paralyzed limbs [59] but also enhances the capability of the spinal cord to translate sensory information into muscle activity for achieving specific motor function, e.g. standing and walking [62]. In addition, recent research has

demonstrated that the biomimetic electrical waveform outperforms the conventional periodic pulses. An EMG-mimetic waveform increases both spinal cord excitability and spinally-induced responses more than the conventional approach [14].

In spite of promising research results, the development of the implantable system used for epidural stimulation for restoring the motor function of the paralyzed is still limited. The implant for motor function recovery must be able to adjust the stimulation patterns (e.g., stimulation intensity, location, pulse width, polarity, and frequency) in real-time in response to the subject's varying walking state [63]. This requires the implantable stimulator to support stimulation with a high channel count in order to target different motor neuron pools in the spinal cord. Furthermore, the stimulator should have the capabilities of independent control for each individual channel and real-time adjustment of the stimulation parameter. Although efforts have been devoted to developing research devices for implantable stimulation, many might not be appropriate for the application of motor function recovery. A device was presented for epidural stimulation in chronically implanted rat, yet the device relied on discrete wires for the communication with the implant, which imposed a risk of infection on the subject and increased the complexity of the surgical procedure [64]. Another device demonstrated the capability of wireless power and data transmission [65], however, it only supported two stimulation channels, which was insufficient to target different motor neuron pools for initiating motor functions. Recent human clinical experiments still relied on commercial implantable stimulators [13, 66] that were not specifically designed for motor function recovery. For example, [13] was designed for deep brain stimulation while [66] was for spinal cord stimulation for pain suppression. Both stimulators are bulky and have limited

programmability, e.g. they only supported stimulation with pre-loaded parameters. This incapability of adjusting the stimulation parameter in real-time limited the effectiveness of motor function recovery. Moreover, those commercialized devices can only support regular and periodic pulses. This limitation impedes the usage of stimulator to generate a more effective stimulation patterns for epidural stimulation, e.g. EMG pattern for increasing both spinal cord excitability and spinally-induced responses [14].

The developed implantable system described in Chapter 2 was tailored for epidural stimulation to fill the technology gap (Figure 38). The implant and coils are implanted subcutaneously. The flexible electrode array is inserted into epidural space for spinal cord stimulation while the EMG wire electrodes are sutured to the leg muscles for kinetics recording. The rat carries a rendezvous device (RD) that wirelessly powers the implant, and serves as a link between the implant and a remote control device.

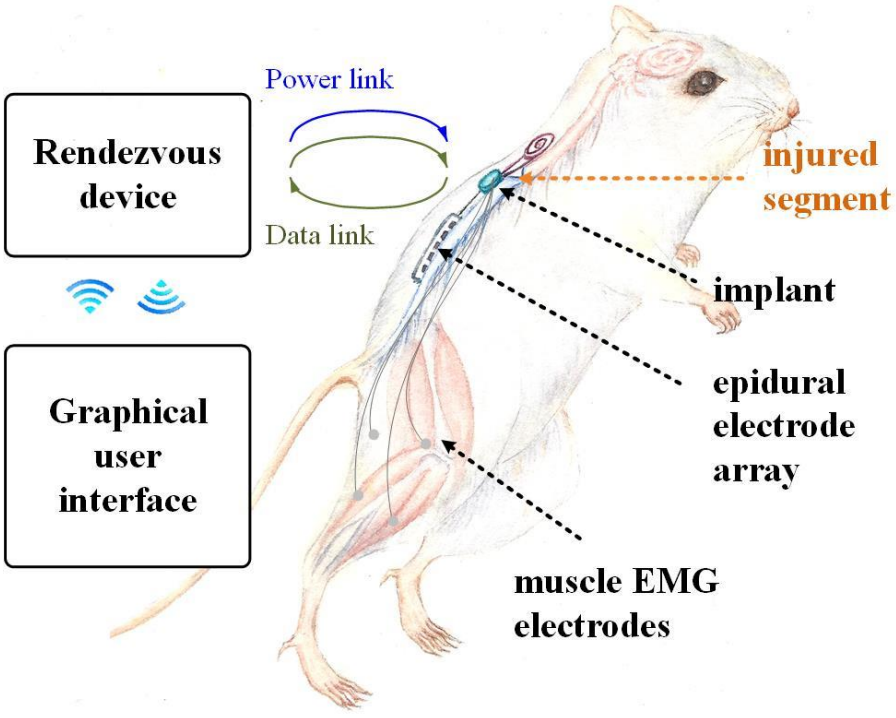

Figure 38. Conceptual illustration of the implantable system for motor function recovery using a rat model [54].

Two *in-vivo* acute tests using rat model are presented in this chapter: 1) epidural stimulation using the implantable system, which demonstrates the selective muscle activation through regular electrical pulses on different spinal neuron pools; 2) epidural stimulation using the biomimetic stimulation system, which quickly validates the effectiveness of EMG-mimetic stimulation waveform for lowering the activation threshold of the motor neurons. Those two preliminary tests are preambles to future *in-vivo* chronic experiments to validate closed-loop biomimetic stimulation using the implantable system for the spinal cord injured.

5.2 *IN-VIVO* ACUTE EXPERIMENT: SELECTIVE MUSCLE ACTIVATION USING IMPLANTABLE SYSTEM

In-vivo acute tests using healthy adult Sprague Dawley rats were conducted to validate the implantable system's capability of selective muscle activation. All procedures complied with the National Institutes of Health Guide for the Care and Use of Laboratory Animals approved by the Animal Research Committee at UCLA. The implant was placed over the lumbosacral spinal cord. The flexible electrode array was inserted in the epidural space to perform electrical stimulation. Eight channels of hindlimb EMG were implanted and connected to a data acquisition system. It also should be mentioned that commercial EMG recording equipment was used in this preliminary acute test. The reverse link operation of the implant for wireless EMG recording will be conducted in the future.

The implant system was able to generate stimulation pulses on 12 out of 12 electrodes and the hindlimb EMG induced by stimuli generated by the implant was recorded successfully. Figure 39 shows one representative stimulation waveform

monitored by the oscilloscope. The stimulus was a biphasic current pulse with an intensity of 50 μA and a pulse width of 0.2 ms. The blue trace was the stimulation command sent from the MCU in the rendezvous device while the green trace was the command demodulated by the DPSK receiver inside the implant. The pink trace was the stimulation output generated by the implant. This output waveform provided the information of the electrode-tissue interface impedance modeled by Randles cell. With a known parameter of the current stimulus (50 μA, 0.2 ms) and the recorded voltage waveform (pink trace), it can be calculated that the interface had a solution resistance (R_s) of 10 kΩ and a double layer capacitance (C_{dl}) of 10 nF by using a time-domain impedance characterization method [56]. The stimulation waveform was also an indication of a fully functional wireless implant system that successfully integrated the GUI on a tablet, the rendezvous, and the implant.

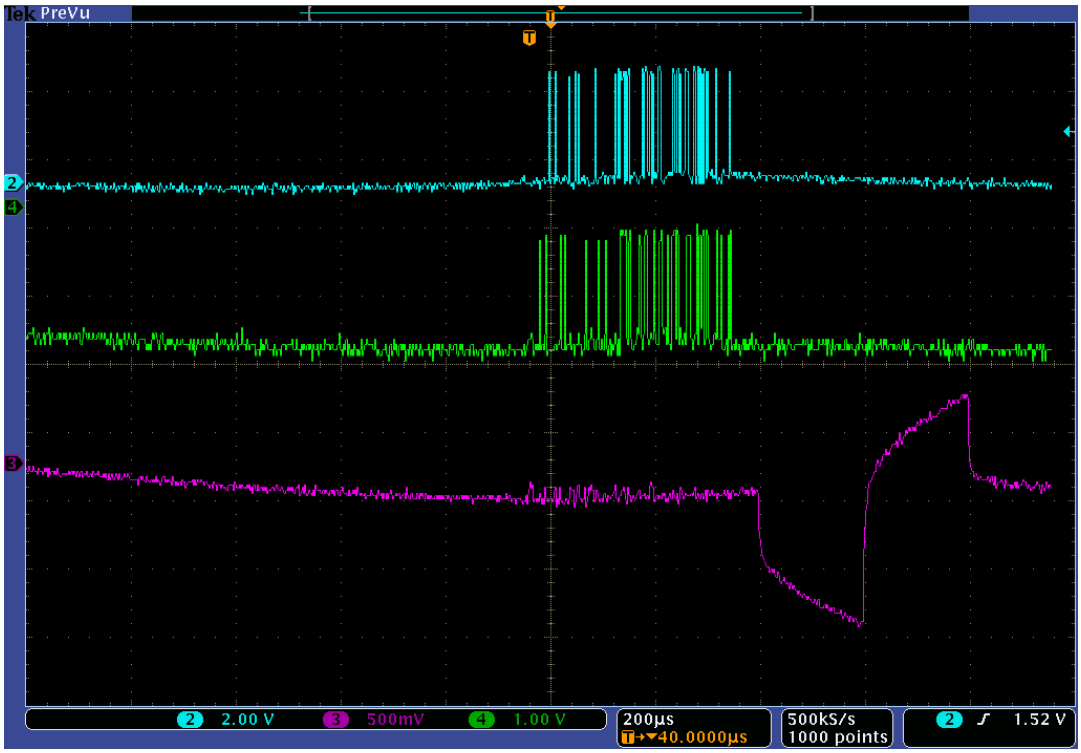

Figure 39. One stimulation event monitored by the oscilloscope.

The implantable system also demonstrated its capability of selective muscle activation (Figure 40). The 12-channel array was placed over the spinal cord, covering L2 to S1 spinal levels. This placement enabled the delivering of stimuli to motor neuron pools for activating tibialis anterior (TA) and soleus (Sol) muscles. Four electrodes at the corner of the array were used to achieve four different bipolar stimulation protocols by combining electrodes. The protocols included left and right limb activation with current polarity from rostral to caudal (Figure 40(a)) and from caudal to rostral (Figure 40(b)). The current flow and the representative recorded single EMG of the left limb stimulation are highlighted in blue while the ones of the right limb stimulation are highlighted in green. The recorded EMG indicated that the left and right limbs both only reacted to the stimuli that were delivered to the neuron pools at their side. In addition, the stimulation delivered to rostral (Figure 40(a)) activated only TAs, while stimulating caudal (Figure 40(b)), responses were elicited also from Sol muscles, which was in good accordance with the rostral/caudal localization of TA and Sol motor pools. This experimental result not only validated the functionality of the implantable system but also demonstrated its capability of selective muscle activation, which was crucial for the future development of closed-loop epidural stimulation.

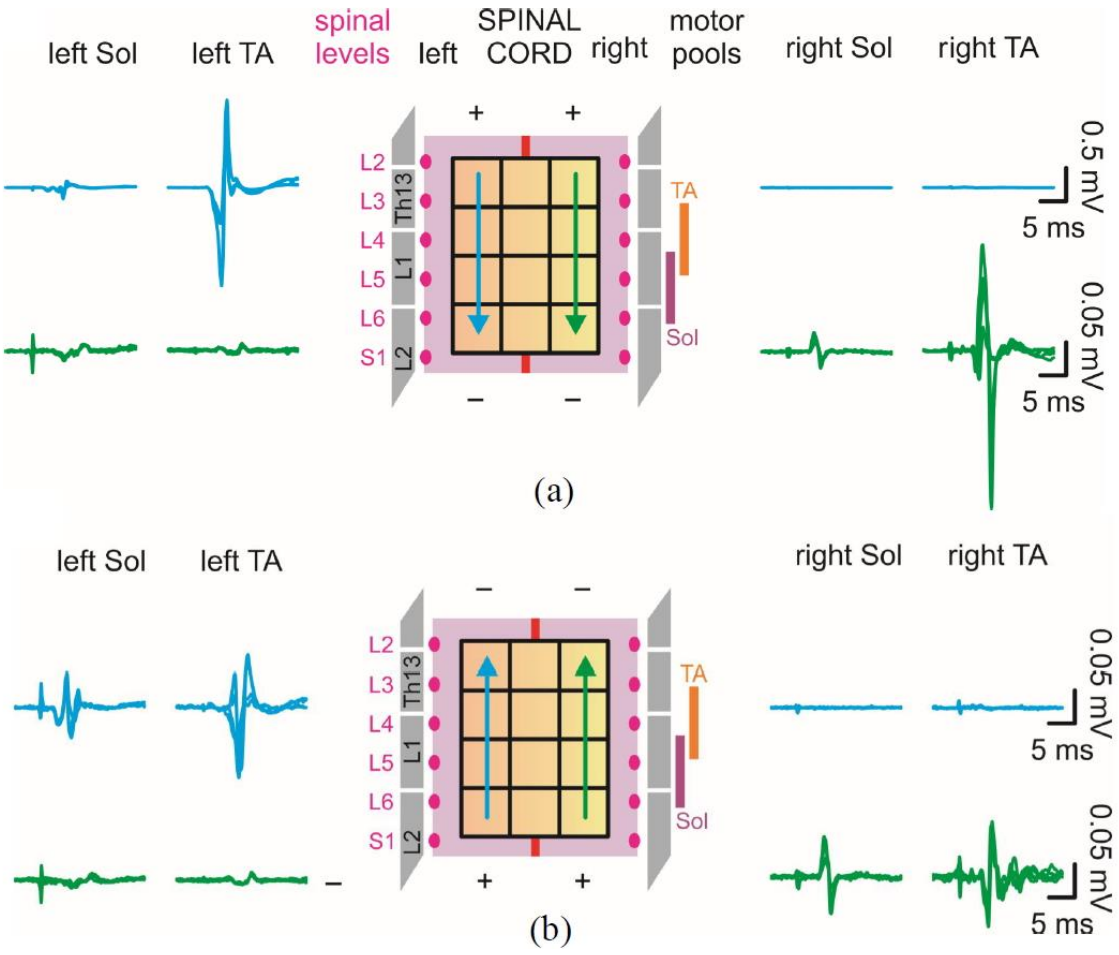

Figure 40. Stimulation setting with a calibrated representation of the electrode array width and the distance between dorsal roots and the representative recorded single EMG. (a) Stimulation was delivered from rostral to caudal. (b) Stimulation was delivered from caudal to rostral.

5.3 *In-Vivo* Acute Experiment: EMG-Mimetic Stimulation Using Biomimetic Stimulation System

An *In-vivo* acute test using a spinally transected adult Long Evans rat was conducted. This test examined the effectiveness of EMG-mimetic waveform generated by the developed biomimetic stimulation system to increase the excitability of spinal neurons. All experimental procedures complied with the National Institutes of Health Guide for the Care and Use of Laboratory Animals approved by the Animal Research Committee at UCLA.

The illustration of the experimental setup is shown in Figure 41. Three types of stimulation were delivered. First, a pulse train (0.3 Hz) at threshold intensity was continuously applied to the dorsal spinal cord. During a short period in the 0.3 Hz tonic stimulation, the EMG-mimetic waveform was applied over four spinal segments. The EMG-mimetic waveform that mimics the Sol muscle of a neurologically intact adult rat during walking was generated by the biomimetic stimulation system presented in Chapter 2. The induced EMG in response to the stimulation was recorded from extensor (tibialis anterior, TA) and flexor (soleus, Sol) muscles through bipolar wire EMG electrodes. The detailed stimulation setting is shown in Figure 42. The spinal cord was transected at Th10 vertebral level. The 18-channel electrode developed by our group [19] was laid on top of the spinal cord, covering L1 to S2 spinal levels. Those spinal levels contain the motor neuron pools that are required to activate TA and Sol muscles. The tonic stimulation was bipolarly delivered to L5 and L6 segments. Two identical but with timing shift (0.5 sec) EMG-mimetic waveforms were bipolarly applied to L1 and S2 segments with opposite polarity. This stimulation protocol repeated the one used in our prior study [14].

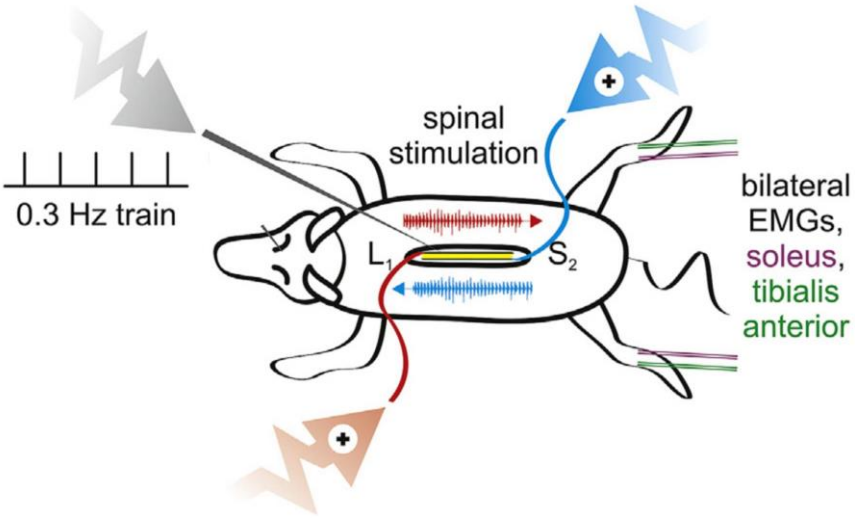

Figure 41. Illustration of the experimental setup of EMG-mimetic stimulation. Adapted from [14].

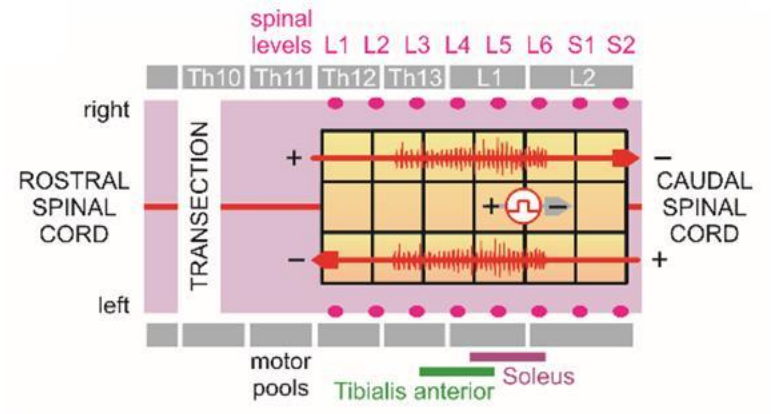

Figure 42. Stimulation setting with a calibrated representation of the electrode array width and the distance between dorsal roots. Adapted from [14].

The EMG-mimetic stimulation (EMS) enhanced spinal network excitability after an acute spinal transection (Figure 43). Before EMS was delivered, the 0.3 Hz tonic stimuli barely activated the hindlimb muscles including right and left Sol and TA (rSol, rTA, lSol, lTA), as shown in Figure 43(a). Representative recorded single EMGs and the time period of those EMGs being recorded are highlighted in blue. During the 30 seconds of EMS (highlighted in orange), strong stimulation artifacts were observed, indicating that the EMG-mimetic waveform was being delivered. After EMS was delivered and terminated (time period highlighted in green), the hindlimb muscles started to react to the 0.3 Hz tonic stimuli. The representative recorded single EMGs (highlighted in green) were much stronger than the ones recorded pre-EMS. Figure 43 (b) shows the amplitude of each recorded EMG in response to 0.3 Hz tonic stimuli during the whole protocol. The amplitude of the EMG increased after EMS for all hindlimbs, which implied that EMS decreased the threshold for activating the motor neurons that innervate those hindlimb muscles. This result is consistent with our prior study [14], whose EMS was delivered by a bulky commercial stimulator. This result also validated the functionality of the developed biomimetic stimulation system.

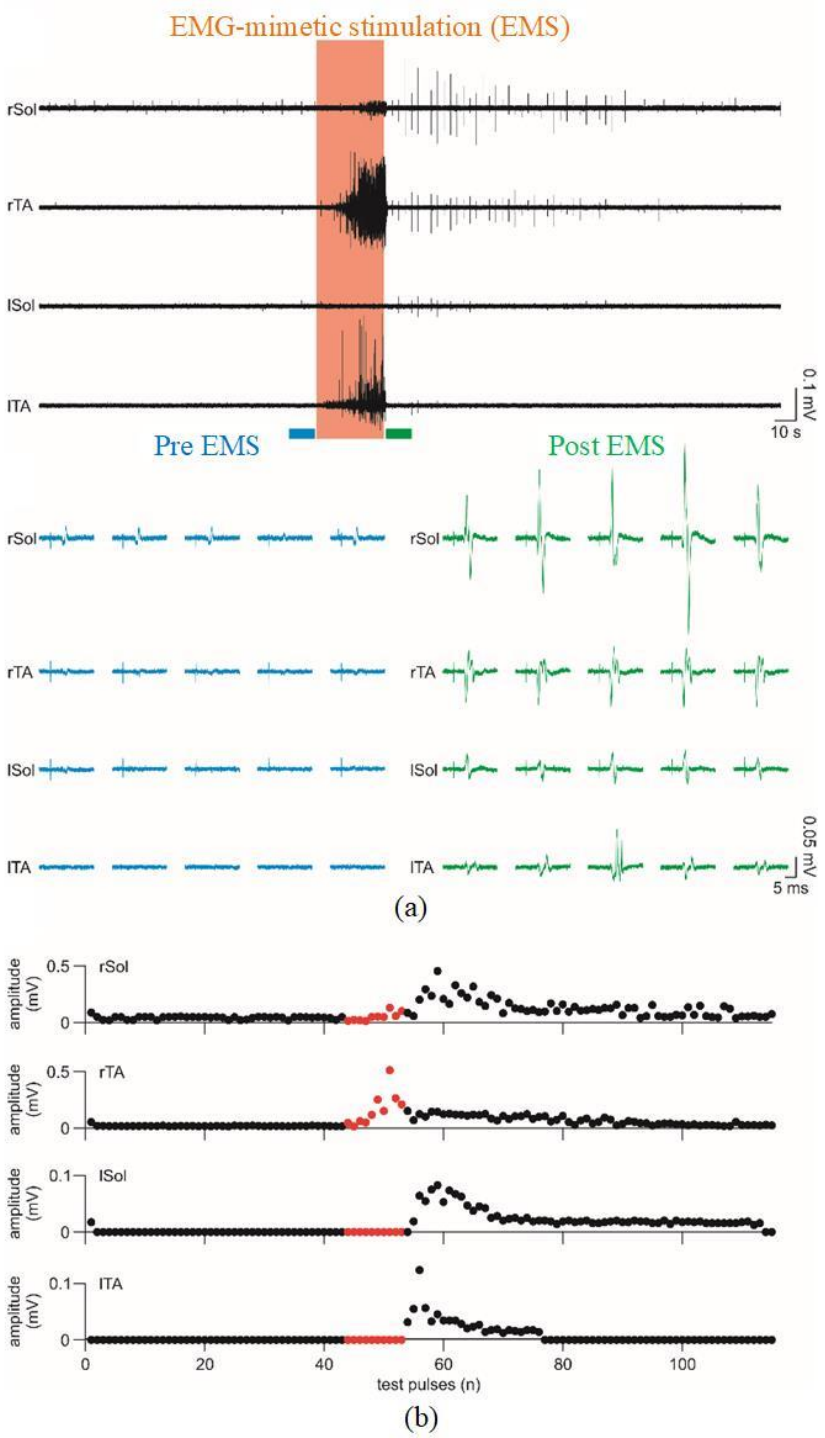

Figure 43. (a) Recorded EMG waveform. The zoom-in view shows the representative EMG before and after EMG-mimetic stimulation. (b) The amplitude of each recorded EMG during the protocol.

Chapter 6
Conclusion and Future Work

Two wireless biomimetic systems including an implantable stimulation and recording system and a biomimetic stimulation system were designed and implemented. The core of the two systems is a versatile system on a chip (SoC) that supports wireless powering, wireless bi-directional data telemetry, and multi-channel biomimetic stimulation and recording. In the implantable stimulation and recording system, the SoC is integrated with a polyimide-based electrode array into a miniaturized implant via a novel heterogeneous packaging approach. The miniaturized implant is powered and configured by the custom-made rendezvous device (RD) and graphical user interface (GUI) through a two-level wireless transmission scheme. This transmission scheme allows remote control of the system in meter range while delivering power and command to the implant inside the body. The system architecture also allows the implementation of the closed-loop control algorithm at the external side, which enables researchers to update the algorithm tailored for various needs. On the other hand, in the biomimetic stimulation system, the SoC is QFP-packaged and integrated with off-the-shelf components into a portable, single battery-powered, and wireless system. This system offers a convenient and reliable platform for quick evaluation of various biomimetic stimulation patterns on animal models.

Both systems were tested and validated in bench-top tests as well as pre-clinical *in-vivo* experiments. *In-vitro* aging tests were also conducted for the implantable system, which validated its capability of chronic implantation for a four-week duration. The

implantable system was tailored for two different *in-vivo* experiments: 1) intestinal stimulation for facilitating gastrointestinal motility using porcine models, and 2) epidural stimulation for selective muscle activation using rat models. In the intestinal stimulation experiment, the system demonstrated its potential for improving GI motility. An effective and safe stimulation protocol for accelerating the intestinal transit was obtained and validated in the acute test. The protocol has a shorter pulse width and a smaller intensity compared with other works for facilitating GI motility [42-44, 46, 47], which is beneficial for the implantable device in terms of power consumption and stimulation safety. The implantable system delivering the proposed protocol likely facilitated the GI motility in the preliminary chronic study. In order to get statistically significant results, a study involving more subjects should be conducted in the future. In the epidural stimulation experiment, the system clearly demonstrated the feasibility of selectively activating the targeted muscle through stimulating proper spinal neuron pools. The induced muscles are right and left tibialis anterior (TA) and soleus (Sol) for standing and walking. This selective muscle activation lays the foundation for the future development of closed-loop epidural stimulation for restoring motor functions. On the other hand, the biomimetic stimulation system was validated *in-vivo* through epidural stimulation using rat models. The EMG-mimetic stimulation pattern generated by the system increased the spinal network excitability in the spinally transected rat, which demonstrated its potential of accelerating the rate of functional recovery after a severe spinal lesion.

The development of the two wireless biomimetic systems paves the way for the realization of an implantable neuromodulation device that supports closed-loop biomimetic stimulation. One future work towards the realization of such a system is

advancing the software and firmware in the current implantable system. The microcontroller (MCU) firmware in the rendezvous device (RD) will be upgraded to support the biomimetic stimulation feature while a sophisticated closed-loop control algorithm will be realized in the graphical user interface (GUI). Note that the upgrade of MCU firmware in the implantable system will benefit from the knowledge accumulated in the MCU firmware design in the biomimetic stimulation system. Meanwhile, more biological experiments using both developed systems will be conducted in the future. The *in-vivo* data acquired in biological experiments will be insightful for the development of a closed-loop control algorithm, e.g. the closed-loop epidural stimulation for motor function recovery will require more *in-vivo* data of selective muscle activation as presented in Chapter 5. Moreover, the biological experiments will allow us not only to validate biomimetic stimulation patterns reported recently [9-11, 14, 24] but also to explore novel biomimetic waveforms that are more effective than conventional periodic pulses in various applications.

References

[1] T. Cameron, "Safety and efficacy of spinal cord stimulation for the treatment of chronic pain: a 20-year literature review," *Journal of Neurosurgery: Spine,* vol. 100, pp. 254-267, 2004.

[2] H. C. Gonzalez and V. Velanovich, "Enterra® Therapy: gastric neurostimulator for gastroparesis," *Expert Review of Medical Devices,* vol. 7, pp. 319-332, 2010.

[3] M. Camilleri, J. Toouli, M. Herrera, B. Kulseng, L. Kow, J. Pantoja, *et al.*, "Intra-abdominal vagal blocking (VBLOC therapy): clinical results with a new implantable medical device," *Surgery,* vol. 143, pp. 723-731, 2008.

[4] K. Famm, B. Litt, K. J. Tracey, E. S. Boyden, and M. Slaoui, "Drug discovery: a jump-start for electroceuticals," *Nature*, vol. 496, pp. 159-161, 2013.

[5] D. Fox, "The shock tactics set to shake up immunology," *Nature,* vol. 545, p. 20, 2017.

[6] E. Waltz, "A spark at the periphery," *Nature Biotechnology,* vol. 34, pp. 904-908, 2016.

[7] M. D. Serruya, N. G. Hatsopoulos, L. Paninski, M. R. Fellows, and J. P. Donoghue, "Brain-machine interface: Instant neural control of a movement signal," *Nature*, vol. 416, p. 141, 2002.

[8] P. J. Grahn, G. W. Mallory, B. M. Berry, J. T. Hachmann, D. A. Lobel, and J. L. Lujan, "Restoration of motor function following spinal cord injury via optimal

control of intraspinal microstimulation: toward a next generation closed-loop neural prosthesis," *Frontiers in Neuroscience,* vol. 8, p. 296, 2014.

[9] F. Dose, R. Menosso, and G. Taccola, "Rat locomotor spinal circuits in vitro are activated by electrical stimulation with noisy waveforms sampled from human gait," *Physiological Reports,* vol. 1, 2013.

[10] D. T. Brocker, B. D. Swan, D. A. Turner, R. E. Gross, S. B. Tatter, M. M. Koop, *et al.*, "Improved efficacy of temporally non-regular deep brain stimulation in Parkinson's disease," *Experimental Neurology,* vol. 239, pp. 60-67, 2013.

[11] A. Soto-Breceda, T. Kameneva, H. Meffin, M. Maturana, and M. Ibbotson, "Irregularly timed electrical pulses reduce adaptation of retinal ganglion cells," *Journal of Neural Engineering,* vol. 15, p. 056017, 2018.

[12] E. Musk, "An integrated brain-machine interface platform with thousands of channels," *BioRxiv,* p. 703801, 2019.

[13] F. B. Wagner, J.-B. Mignardot, C. G. Le Goff-Mignardot, R. Demesmaeker, S. Komi, M. Capogrosso, *et al.*, "Targeted neurotechnology restores walking in humans with spinal cord injury," *Nature,* vol. 563, p. 65, 2018.

[14] G. Taccola, P. Gad, S. Culaclii, R. M. Ichiyama, W. Liu, and V. R. Edgerton, "Using EMG to deliver lumbar dynamic electrical stimulation to facilitate cortico-spinal excitability," *Brain Stimulation,* 2019.

[15] L. Kapural, C. Yu, M. W. Doust, B. E. Gliner, R. Vallejo, B. T. Sitzman, *et al.*, "Novel 10-kHz high-frequency therapy (hf10 therapy) is superior to traditional low-frequency spinal cord stimulation for the treatment of chronic back and leg

pain: The SENZA-RCT randomized controlled trial," *Anesthesiology: The Journal of the American Society of Anesthesiologists,* vol. 123, pp. 851-860, 2015.

[16] Y.-K. Lo, Y.-C. Kuan, S. Culaclii, B. Kim, P.-M. Wang, C.-W. Chang, *et al.*, "A Fully Integrated Wireless SoC for Motor Function Recovery After Spinal Cord Injury," *IEEE Transactions on Biomedical Circuits and Systems,* vol. 11, pp. 497-509, 2017.

[17] K. Chen, Y.-K. Lo, Z. Yang, J. Weiland, M. S. Humayun, and W. Liu, "A system verification platform for high-density epiretinal prostheses," *Biomedical Circuits and Systems, IEEE Transactions on,* vol. 7, pp. 326-337, 2013.

[18] P.-M. Wang, G. Dubrovsky, J. C. Dunn, Y.-K. Lo, and W. Liu, "A Wireless Implantable System for Facilitating Gastrointestinal Motility," *Micromachines,* vol. 10, p. 525, 2019.

[19] C.-W. Chang, Y.-K. Lo, P. Gad, R. Edgerton, and W. Liu, "Design and fabrication of a multi-electrode array for spinal cord epidural stimulation," in *Engineering in Medicine and Biology Society (EMBC), 2014 36th Annual International Conference of the IEEE,* 2014, pp. 6834-6837.

[20] C. Anand, A. Al-Juburi, B. Familoni, H. Rashed, T. Cutts, N. Abidi, *et al.*, "Gastric electrical stimulation is safe and effective: a long-term study in patients with drug-refractory gastroparesis in three regional centers," *Digestion,* vol. 75, pp. 83-89, 2007.

[21] L. Rodríguez, P. Rodriguez, B. Gómez, J. C. Ayala, D. Oxenberg, A. Perez-Castilla, *et al.*, "Two-year results of intermittent electrical stimulation of the lower

esophageal sphincter treatment of gastroesophageal reflux disease," *Surgery*, vol. 157, pp. 556-567, 2015.

[22] G. A. Kendir, W. Liu, G. Wang, M. Sivaprakasam, R. Bashirullah, M. S. Humayun, *et al.*, "An optimal design methodology for inductive power link with class-E amplifier," *Circuits and Systems I: Regular Papers, IEEE Transactions on*, vol. 52, pp. 857-866, 2005.

[23] G. Wang, W. Liu, M. Sivaprakasam, M. Zhou, J. D. Weiland, and M. S. Humayun, "A wireless phase shift keying transmitter with Q-independent phase transition time," in *Engineering in Medicine and Biology Society, 2005. IEEE-EMBS 2005. 27th Annual International Conference of the*, 2006, pp. 5238-5241.

[24] Y. Yang, A. T. Connolly, and M. M. Shanechi, "A control-theoretic system identification framework and a real-time closed-loop clinical simulation testbed for electrical brain stimulation," *Journal of Neural Engineering*, vol. 15, p. 066007, 2018.

[25] "STG4000 Series Stimulus Generators ". Available online: https://www.multichannelsystems.com/products/stg4000-series

[26] "Activa RC Neurostimulator ". Available online: http://www.medtronic.com/us-en/healthcare-professionals/products/neurological/deep-brain-stimulation-systems/activa-rc.html

[27] "Spectra WaveWriter™ SCS System ". Available online: http://www.bostonscientific.com/en-US/products/spinal-cord-stimulator-systems.html

[28] P.-M. Wang, S. Culaclii, W. Yang, Y. Long, J. Massachi, Y.-K. Lo, *et al.*, "A Novel Biomimetic Stimulator System for Neural Implant," in *2019 9th International IEEE/EMBS Conference on Neural Engineering (NER)*, 2019, pp. 843-846.

[29] J. Massachi, Y.-K. Lo, P.-M. Wang, and W. Liu, "A Wireless Platform to Support Pre-Clinical Trial of Neural Implant for Spinal Cord Injury," presented at the *2018 40th Annual International Conference of the IEEE Engineering in Medicine and Biology Society (EMBC)*, Honolulu, HI, USA, 2018.

[30] Y.-K. Lo, K. Chen, P. Gad, and W. Liu, "An On-Chip Multi-Voltage Power Converter With Leakage Current Prevention Using 0.18 m High-Voltage CMOS Process," *Biomedical Circuits and Systems, IEEE Transactions on*, 2015.

[31] W. Franks, I. Schenker, P. Schmutz, and A. Hierlemann, "Impedance characterization and modeling of electrodes for biomedical applications," *Biomedical Engineering, IEEE Transactions on*, vol. 52, pp. 1295-1302, 2005.

[32] P. E. Donaldson, "The encapsulation of microelectronic devices for long-term surgical implantation," *IEEE Transactions on Biomedical Engineering*, pp. 281-285, 1976.

[33] A. F - 07, "Standard Guide for Accelerated Aging of Sterile Barrier Systems for Medical Devices," 2011.

[34] J. E. Hall, *Guyton and Hall textbook of medical physiology*: Elsevier Health Sciences, 2015.

[35] A. F. Peery, S. D. Crockett, C. C. Murphy, J. L. Lund, E. S. Dellon, J. L. Williams, *et al.*, "Burden and cost of gastrointestinal, liver, and pancreatic

diseases in the United States: update 2018," *Gastroenterology,* vol. 156, pp. 254-272, 2018.

[36] K. Sanders, "Regulation of smooth muscle excitation and contraction," *Neurogastroenterology & Motility,* vol. 20, pp. 39-53, 2008.

[37] J. D. Huizinga and W. J. Lammers, "Gut peristalsis is governed by a multitude of cooperating mechanisms," *American Journal of Physiology-Gastrointestinal and Liver Physiology,* vol. 296, pp. G1-G8, 2009.

[38] N. Valentin, A. Acosta, and M. Camilleri, "Early investigational therapeutics for gastrointestinal motility disorders: from animal studies to Phase II trials," *Expert Opinion on Investigational Drugs,* vol. 24, pp. 769-779, 2015.

[39] K. M. Sanders, S. D. Koh, and S. M. Ward, "Interstitial cells of Cajal as pacemakers in the gastrointestinal tract," *Annu. Rev. Physiol.*, vol. 68, pp. 307-343, 2006.

[40] R. K. Goyal and I. Hirano, "The enteric nervous system," *New England Journal of Medicine,* vol. 334, pp. 1106-1115, 1996.

[41] J. B. Furness, "The enteric nervous system and neurogastroenterology," *Nature Reviews Gastroenterology & Hepatology*, vol. 9, p. 286, 2012.

[42] R. W. McCallum, J. D. Z. Chen, Z. Lin, B. D. Schirmer, R. D. Williams, and R. A. Ross, "Gastric pacing improves emptying and symptoms in patients with gastroparesis," *Gastroenterology,* vol. 114, pp. 456-461, 1998.

[43] Z. Lin, I. Sarosiek, J. Forster, R. A. Ross, J. D. Chen, and R. W. McCallum, "Two - channel gastric pacing in patients with diabetic gastroparesis," *Neurogastroenterology & Motility,* vol. 23, pp. 912-e396, 2011.

[44] J. Yin and J. D. Chen, "Excitatory effects of synchronized intestinal electrical stimulation on small intestinal motility in dogs," *American Journal of Physiology-Gastrointestinal and Liver Physiology*, vol. 293, pp. G1190-G1195, 2007.

[45] G. Dubrovsky, Y.-K. Lo, P.-M. Wang, M.-D. Wu, N. Huynh, W. Liu, *et al.*, "Intestinal Electrical Stimulation to Increase the Rate of Peristalsis," *Journal of Surgical Research*, vol. 236, pp. 153-158, 2019.

[46] S. Chen, Y. Li, S. Yao, Y. Zhang, L. Liu, X. Guo, *et al.*, "Implantable colonic electrical stimulation improves gastrointestinal transit and defecation in a canine constipation model," *Neuromodulation: Technology at the Neural Interface*, vol. 19, pp. 108-115, 2016.

[47] H. Sallam and J. Chen, "Colonic electrical stimulation: potential use for treatment of delayed colonic transit," *Colorectal Disease*, vol. 15, pp. e244-e249, 2013.

[48] J. Volkmann, J. Herzog, F. Kopper, and G. Deuschl, "Introduction to the programming of deep brain stimulators," *Movement disorders: official journal of the Movement Disorder Society*, vol. 17, pp. S181-S187, 2002.

[49] B. Hershey, C. Valencia, and T. L. Yearwood, "Pulse width programming in spinal cord stimulation: a clinical study," *Pain Physician*, vol. 13, pp. 321-335, 2010.

[50] A. Mertens, R. Raedt, S. Gadeyne, E. Carrette, P. Boon, and K. Vonck, "Recent advances in devices for vagus nerve stimulation," *Expert Review of Medical Devices*, vol. 15, pp. 527-539, 2018.

[51] S. Liu and J. Chen, "Colonic electrical stimulation regulates colonic transit via the nitrergic pathway in rats," *Digestive Diseases and Sciences,* vol. 51, pp. 502-505, 2006.

[52] C. Sevcencu, N. J. Rijkhoff, and T. Sinkjaer, "Colon emptying induced by sequential electrical stimulation in rats," *IEEE Transactions on Neural Systems and Rehabilitation Engineering,* vol. 13, pp. 516-523, 2005.

[53] R. W. McCallum, W. Snape, F. Brody, J. Wo, H. P. Parkman, and T. Nowak, "Gastric electrical stimulation with Enterra therapy improves symptoms from diabetic gastroparesis in a prospective study," *Clinical Gastroenterology and Hepatology,* vol. 8, pp. 947-954. e1, 2010.

[54] W. Liu, P.-M. Wang, and Y.-K. Lo, "Towards closed-loop neuromodulation: a wireless miniaturized neural implant SoC," in *SPIE Defense+ Security*, 2017, pp. 1019414-1019414-8.

[55] X. Lin, J. Hayes, L. Peters, and J. Chen, "Entrainment of intestinal slow waves with electrical stimulation using intraluminal electrodes," *Annals of Biomedical Engineering,* vol. 28, pp. 582-587, 2000.

[56] Y.-K. Lo, C.-W. Chang, and W. Liu, "Bio-impedance characterization technique with implantable neural stimulator using biphasic current stimulus," in *Engineering in Medicine and Biology Society (EMBC), 2014 36th Annual International Conference of the IEEE,* 2014, pp. 474-477.

[57] N. H. White and N. H. Black, "Spinal Cord Injury Facts and Figures at a Glance," 2017.

[58] S. Harkema, Y. Gerasimenko, J. Hodes, J. Burdick, C. Angeli, Y. Chen, *et al.*, "Effect of epidural stimulation of the lumbosacral spinal cord on voluntary movement, standing, and assisted stepping after motor complete paraplegia: a case study," *The Lancet,* vol. 377, pp. 1938-1947, 2011.

[59] C. A. Angeli, V. R. Edgerton, Y. P. Gerasimenko, and S. J. Harkema, "Altering spinal cord excitability enables voluntary movements after chronic complete paralysis in humans," *Brain,* vol. 137, pp. 1394-1409, 2014.

[60] E. M. Moraud, J. Zitzewitz, J. Miehlbradt, S. Wurth, E. Formento, J. DiGiovanna, *et al.*, "Closed-loop control of trunk posture improves locomotion through the regulation of leg proprioceptive feedback after spinal cord injury," *Scientific Reports,* vol. 8, p. 76, 2018.

[61] M. L. Gill, P. J. Grahn, J. S. Calvert, M. B. Linde, I. A. Lavrov, J. A. Strommen, *et al.*, "Neuromodulation of lumbosacral spinal networks enables independent stepping after complete paraplegia," *Nature Medicine,* vol. 24, p. 1677, 2018.

[62] C. A. Angeli, M. Boakye, R. A. Morton, J. Vogt, K. Benton, Y. Chen, *et al.*, "Recovery of over-ground walking after chronic motor complete spinal cord injury," *New England Journal of Medicine,* vol. 379, pp. 1244-1250, 2018.

[63] M. Capogrosso, F. B. Wagner, J. Gandar, E. M. Moraud, N. Wenger, T. Milekovic, *et al.*, "Configuration of electrical spinal cord stimulation through real-time processing of gait kinematics," *Nature Protocols,* vol. 13, p. 2031, 2018.

[64] V. Giagka, C. Eder, N. Donaldson, and A. Demosthenous, "An implantable versatile electrode-driving ASIC for chronic epidural stimulation in rats," *IEEE Transactions on Biomedical Circuits and Systems,* vol. 9, pp. 387-400, 2014.

[65] Q. Xu, D. Hu, B. Duan, and J. He, "A fully implantable stimulator with wireless power and data transmission for experimental investigation of epidural spinal cord stimulation," *IEEE Transactions on Neural Systems and Rehabilitation Engineering*, vol. 23, pp. 683-692, 2015.

[66] D. G. Terson de Paleville, S. J. Harkema, and C. A. Angeli, "Epidural stimulation with locomotor training improves body composition in individuals with cervical or upper thoracic motor complete spinal cord injury: A series of case studies," *The Journal of Spinal Cord Medicine*, vol. 42, pp. 32-38, 2019.